2017

Cathode Interface Engineering for High Performance Planar Perovskite Solar Cells

MD Nazmul Hasan
South Dakota State University

CATHODE INTERFACE ENGINEERING FOR HIGH PERFORMANCE PLANAR PEROVSKITE SOLAR CELLS

BY

MD NAZMUL HASAN

A thesis submitted in partial fulfillment of the requirements for the

Master of Science

Major in Electrical Engineering

South Dakota State University

2017

CATHODE INTERFACE ENGINEERING FOR HIGH PERFORMANCE PLANAR PEROVSKITE SOLAR CELLS

MD NAZMUL HASAN

This thesis is approved as a creditable and independent investigation by a candidate for the Master of Science degree and is acceptable for meeting the thesis requirements for this degree. Acceptance of this thesis does not imply that the conclusions reached by the candidate are necessarily the conclusions of the major department.

Qiquan Qiao, Ph.D. Date
Thesis Advisor

Steven Hietpas, Ph.D. Date
Head, Department of Electrical Engineering and Computer Science

Michel C. Doerner Ph.D. Date
Dean, Graduate School

ACKNOWLEDGEMENTS

The work presented in this thesis was supported from NSF MRI (grant no. 1229577), the grants including NASA EPSCoR (NNX13AD31A), SDSU MS program and by the State of South Dakota.

I convey my sincere gratitude to Dr. Qiquan Qiao for advising me the academic courses and research works. I am thankful to him to work as a graduate research assistant at the Center for Advanced Photovoltaics, South Dakota State University. I would like to thank Dr. Steven Hietpas for giving me a chance to work as a graduate teaching assistant for financial support in my study. The guidance and support from Dr. Qiao have been crucial throughout the course work and research in enhancing the quality of this thesis.

I would also like to acknowledge my thesis committee members, Dr. Zhen Ni and Dr. Gary Hatfield and Mary Bowne for their time and effort on revising my thesis. I am grateful to Khan Mamun Reza, Sally Mabrouk, Nirmal Adhikari, Ashish Dubey, Wenfeng Zhang, Hytham Elbohy, Ashim Gurung and Behzad Bahrami for their support and encouragement in research.

Finally, I would like to thank my family and friends for their love and support.

TABLE OF CONTENTS

LIST OF FIGURES

LIST OF TABLES

ABSTRACT

CATHODE INTERFACE ENGINEERING FOR HIGH PERFORMANCE PLANAR PEROVSKITE SOLAR CELLS

MD NAZMUL HASAN

2017

Organic-inorganic hybrid perovskite solar cells (PSCs) have already improved their power conversion efficiency (PCE) from 3.9% to ~22.1% at present. This demonstrated that PSCs can be a promising alternative to conventional silicon solar cells. PSCs have been marked as one of the most favorable next-generation solar cells due to their high extinction coefficient, broad light absorption range and ambipolar charge transport properties, low production cost, and simple fabrication processing. Various device architectures have been designed and investigated for constructing high performance PSCs consisting of different electron transport layers (ETL) and hole transport layers (HTL). In general, PSCs are fabricated in two structures: mesoporous scaffold n-i-p and planar heterojunction p-i-n PSCs. Although mesoscopic PSCs have obtained an impressive PCE, it requires high temperature process (> 450^{o}C) for forming compact TiO_2 and mesoporous TiO_2 that hinders their applications that require mechanical flexibility. On the other hand, planar p-i-n PSCs have drawn attention due to low temperature processing, mechanical flexible devices.

The goal of this work is to introduce a non-conjugated polymer material Polyvinylpyrrolidone (PVP) as cathode buffer layer (CBL) and understand interfacial engineering in planar p-i-n PSCs. PVP was used for the first time as a CBL in PSCs. The ETL and HTL are highly responsible to increase carrier separation, improve charge

collection and reduce recombination. Additionally, the buffer layer between ETL and metal cathode (like Ca, Al, Ag) electrode in PSCs plays a crucial role in energy-level alignment, trap state passivation and PSCs film morphology.

A comparative study on PSCs without and with CBL was investigated where rhodamine as CBL was considered for control device. The thickness of PVP CBL was analyzed by changing spin speed from 1000 rpm to 5000 rpm at an interval of 2000 rpm. The optimal spin speed was found at 3000 rpm, which achieved an average efficiency of 15.30%. The concentrations of PVP dissolved in isopropanol was optimized from 0.5 mg/ml to 2.0 mg/ml. There was simultaneous enhancement of short circuit current density (J_{sc}), open circuit voltage (V_{oc}), fill factor (FF), and overall power conversion efficiency (PCE) due to incorporation of PVP. The best device achieved a PCE of 16.35%. Various device characterizations such as atomic force microscopy (AFM), scanning electron microscopy (SEM) etc. were performed to interpret the enhancement of device performance.

Chapter 1. Introduction

1.1 Background

In order to generate electricity for homes, schools, businesses and factories, different energy resources are needed. Energy sources such as solar, hydro, wind, fossil fuels etc. are highly preferable to make life easier and comfortable. The need of energy supply is increasing with the rapid growth of world population. As reported by international energy agency (IEA) data analysis, fossil fuels such as oil, coal and natural gasses are main energy sources of producing energy in the world. They cover almost 66% of the energy market. Recent days, the world's total energy consumption has been doubled [1]. Figure 1.1 shows fuel energy consumed in million tons of oil equivalent (Mtoe) in 1973 and 2015.

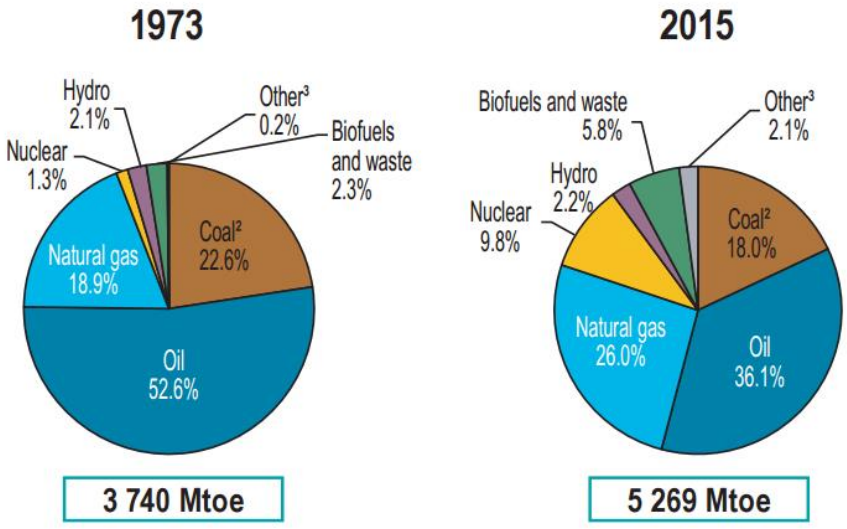

Figure 1. 1 World energy consumption in 2015[1]

Although fossil fuels have lots of advantages, they have serious issues including environmental pollution and greenhouse gas (CO_2, SO_2, NO, poly-aromatic, etc.) emission. It is believed that CO_2 and ozone gas are highly responsible for global warming and dramatic change of weather [1]. In the last two decades, the total CO_2 increased by 43%,

which is expected to rise from 30.2 billion metric tons in 2008 to 35.2 billion metric tons in 2020 [2]. Therefore, it is urgent to use alternate sources of energy such as geothermal, heat, biomass, wind, hydro, tidal waves and solar as future energy generation sources [3] [4].

In order to avoid environmental hazards, at least 67 countries are targeting to have a renewable energy target (RET) policy. The European Union and United States baseline target is 20% by 2020, while the Danish government proposed 30% for 2025. Canada has 9 provincial RETs, but no national target so far [5]. The world's primary renewable energy are produced from wind, hydro, biomass and agricultural waste. Among them, photovoltaics (PV) are one of the fastest and greenest energy technologies. The total energy consumption in the world is around 5.6×10^{20} J annually where the sun delivers 1.7×10^{17} W to the earth. If it is fully utilized with 100% efficiency, then it should take around 55 minutes (5.6×10^{20} Joule/ 1.7×10^{17} W = 55 minutes) to fulfill the requirement. The energy provided by the sun to the earth should be equal to the world's annual energy consumption [6].

Harvesting solar energy can pave a way to clean energy production for the next generation. Figure 1.2 shows solar cell trends over the last few decades certified by the National Renewable Energy Laboratory (NREL) [7].

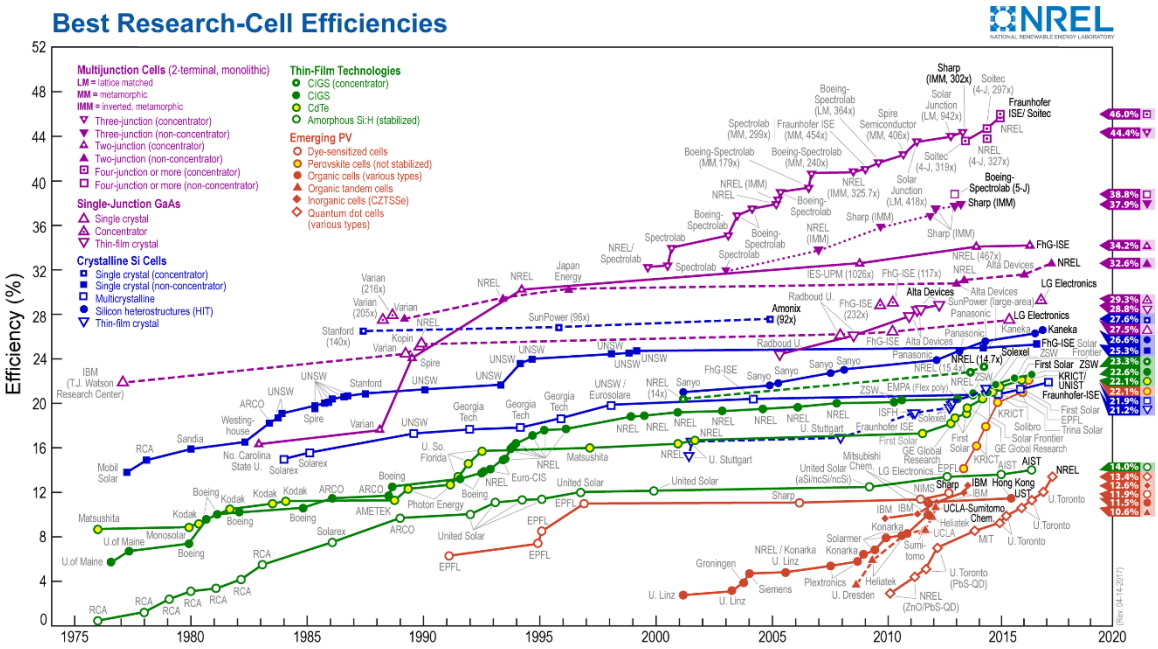

Figure 1. 2 Solar cell trends over last few decades (compiled by National Renewable Energy Laboratory) [7]

The most commercialized solar cells (SCs) are based on Si inorganic. Bell laboratory, first built and demonstrated silicon PV cells in 1954, which was made from single p-n junction Si. Since then, SCs have been classified in three different categories. Single/mono crystalline and poly crystalline silicon (c-Si) are considered as first generation solar cells. Amorphous silicon (a-Si), microcrystalline silicon, copper indium gallium selenide (CIGS), and cadmium telluride (CdTe) are considered as second generation solar cells due to use of thin film technologies. The third generation solar cell includes polymer, oligomers, dye synthesized solar cells (DSSCs), and organic/inorganic hybrid perovskite solar cells (PSCs) which are still under continuous research for further improvement and stability.

Although Si solar cells cover almost 95% of the market over the exiting SCs, it has still some limitations to think alternatively for different solar systems. Most of the cases,

a-Si, and CIGS or CdTe solar cells have the issue of light induced degradation. The Indium and tellurium have the chance of scarcity for mass scale production. These limitations have been eliminated by replacing c-Si solar cell technologies. However, they have the poor light absorption capability due to the use of a few hundred microns thick c-Si film for sufficient light absorption and also suffer from high series resistance which affects the device fill factor and overall performance. High temperature and high vacuum process are also other reason for c-Si technology to make the device costly.

Organic SCs are not like inorganic Si solar cells. Organic photovoltaics (OPVs) added a new dimension to meet the limitations from first and second generation SCs. They introduced a way of first solution process SCs with materials diversity and large scale manufacturing. In addition, they have light weight, low material consumption semi-transparency, less toxicity and device flexibility. However, OPVs have some limitations of low efficiency and organic materials poor stability. Researcher started to develop organic –inorganic hybrid solar cells to overcome these limitations and to utilize the properties of both materials.Dye sensitized Solar cells (DSSC) are also attractive sources of green energy. It is simple in fabrication using conventional roll-printing techniques, high efficiency, semi-transparent and semi-flexible. But the use of expensive platinum or ruthenium and liquid electrolyte presents a serious challenge to making suitable cells for use in all weather.

Recently, a new type of SC called ‘Perovskite’ has surpassed the efficiency limit of OPVs and DSSCs. The structure of an organic-inorganic perovskite has a basic recipe of ABX_3, where A and B are cations and X is a halide atom. New growth methods of fabrications, smooth perovskite film morphology, novel device design and innovations in

material combination lead the perovskite PCE significantly higher compared to the other solution processed SCs. Methylammonium lead triiodide ($MAPbI_3$, $CH_3NH_3PbI_3$) is the most widely used single halide perovskite composition where methylammonium iodide (CH_3NH_3I or MAI) is the organic part which facilitates self-assembly and lead iodide (PbI_2) is the inorganic salt which provides an extended network by covalent or ionic interaction that allows for the precise crystalline structure formation. Figure 1.3 displays the increasing trend in efficiency of perovskite solar cells the last ten years.

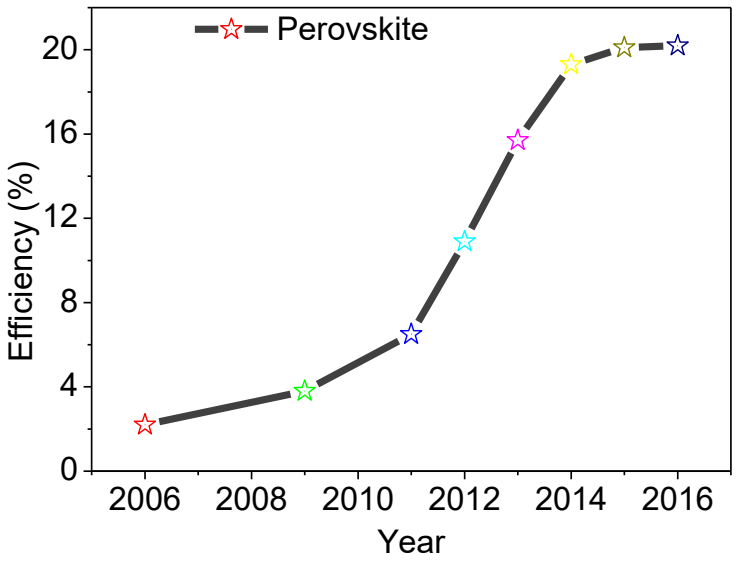

Figure 1. 3 Perovskite efficiency trend in last ten years

PSCs facilitates long-range am-bipolar carrier diffusion length, low exciton binding energy and high absorption coefficient for excellent photovoltaic characteristics.

1.2 Previous work

Alexandre-Edmund Becquerel, a French physicist first demonstrated the photovoltaic phenomenon in 1839. In his experiment, silver bromide (AgBr) or silver chloride (AgCl) was placed in an acetic solution and illuminated light between two

platinum metal electrodes generated voltage and current [4]. In 1883, by depositing a thin gold layer on the top of selenium semiconductor, Fitts *et al.* first showed solid state solar cell [8] . In 1954 Bell Laboratory introduced first crystalline Si solar cell with an efficiency of 6% [9]. Since then, recent technology of PV research boosted the PCE of polycrystalline silicon solar cell to 20.3% and single crystalline solar cell to 24.7% [10].

In 1976, amorphous Si solar cell was developed with a thickness of 1 micron and PCE of 2.4% [11]. This type of solar cell had the degradation problem due continuous light illumination. The leading technologies tried to think differently instead of Si solar cell. In 1981, Kodak made the PCE of 10% from CdTe solar cells [12] and some companies started to commercialize that type of inorganic thin film solar cells. Additionally CIGS solar cell exceeded the 10% efficiency in the year of 1983-1984 but were not commercially available till 1998.

In 1986, Tang *et al.* reported 1% efficiency of bilayer heterojunction organic solar cell with the concept of donor-acceptor [13, 14]. They spin coated bilayer structure of donor-acceptor material on the top of each other. However, the bilayer polymer solar cell efficiency was low because of low excitons diffusion length and donor-acceptor interfacial area [15]. Therefore, in 1995, Yu *et al.* reported a concept of bulk heterojunction polymer solar cells where donor and acceptor materials intermixed to forming large interfacial area for excitons dissociation and charge transport [16]. In 2001, Shaheen *et al.* reported around 2.5% PCE using that concept [17]. It increased excitons dissociation but could not cover the wide range of solar spectrum. In order to overcome this limitation, tandem solar cell concept was introduced. In 2012, Dou *et al.* achieved the efficiency of 8.62% [18] and in 2013 You *et al.* reported the efficiency of 10.6% using

that tandem structure of organic solar cells [19].

In 1987, Moser *et al.* introduced the concept of DSSCs. He demonstrated slightly enhancement of photocurrent due to dye sensitized halogenated silver plates (Ag) [20]. In 1991, O'Regan and Grätzel fabricated DSSCs with PCE of 7.9% in simulated solar light and PCE of 12% in diffused sunlight [21]. Although it's highest efficiency was developed around 12.3 % [22] , it was limited commercially due to use of expensive platinum or ruthenium counter electrode and also presence of liquid electrolyte which hindered to make suitable cell for all weather.

In 2009, Miyasaka *et al.* first introduced perovskite solar cell with PCE of 3.8% [23-25]. Unlike dyes, these perovskite have higher absorption in a thin film of 500nm [26]. They used methylammonium lead iodide ($CH_3NH_3PbI_3$) acting as an absorber layer where iodide/triiodide acting as redox couple. The liquid electrolyte dissolved perovskite film within a minute and became unstable.

In 2012, Park *et al.* was able to fabricate high efficiency PSCs using hole conductor [2, 2 (7, 7)- tetrakis-(N, N dipmethoxyphenylamine) 9, 9 (-spirobifluorene)] (spiro-OMeTAD) that was substituted in liquid electrolyte and obtained PCE of 9.7% [27, 28]. Later on, some research group used mesoporous titanium dioxide (TiO_2) as an ETL. [29]. However, n-i-p structure based PSCs fabricated with a mesoporous TiO_2 as an ETL requires high temperature processing (> 400 ^oC) [30]. Some researcher used three types of layers of TiO_2 as an ETL that causes high resistance in the interface and reduces the device performances.

In 2013, Liu *et al.* reported PCE of 15% for planar PSCs with different technique [24]. They fabricated PSCs using thermal evaporation process which requires very high

vacuum and high energy to evaporate perovskite material. These limitation hindered mass production of PSCs.

In 2014 You *et al.* reported ITO based glass substrate p-i-n structure perovskite solar cells with PCE of 11.5% using a p-type poly (3,4-ethylenedioxythiophene): poly (styrenesulfonate) (PEDOT:PSS) layer as HTL and PCE of 9.2% using polyethylene terephthalate as HTL on the top of the ITO substrate [31, 32].

However planar p-i-n structure based OPVs or PSCs are preferred due to low temperature solution process, less hysteresis and easier to fabricate in than n-i-p structure. The electrical properties of semiconductor devices depends on charge injection and extraction at the metal-organic semiconductor interfaces [33, 34]. To minimize contact barrier, suppress charge recombination, control metals work function and surface energy, better interface between ETL and Ag, is highly required which matches with the LUMO level organic semiconductor. In 2006, Li *et al.* reported metal oxide CBL between polymer bled and Al [35]. Azimi showed comparable study with using ZnO CBL to improve device performance [36].

Few studies have been revealed using non-conjugated insulating polymer as a CBL. In OPVs, Zhang *et al.* first reported to insert a thin layer of a non-conjugated polymer, poly (ethylene oxide) (PEO) as CBL [37]. They found dramatic improvement of V_{oc} due to increase built in potential at the interface and enhancement of FF, J_{sc} as well. Poly [(9,9-bis(3′-(N,N-dimethylamino) propyl)-2,7-fluorene)-alt-2,7-(9,9-dioctylfluorene)] (PFN), poly (ethylene glycol) (PEG), poly (dimethylsiloxane)-block-poly (methyl methacrylate) (PDMS-b-PMMA) and poly (4-hydroxystyrene) (PHS), all were used as optimized CBL

between the active layer of polymer blend and metal electrode (Ag or Al) [38-41]. Most of the cases they reported about enhancement of V_{oc} due to creating build in potential at the interface which controls metal electrode work function (WF), increase of J_{sc} due to produce interface dipole which increases charge transport and suppresses carrier recombination, improvement of FF due to have less series resistance at the interface. However, all the study has been done on OPVs not in PSCs.

Zhang reported perovskite solar cell with PCE 12.01% and 11.28% by inserting two non-conjugated interfacial layer individually, ethoxylated polyethylenimine (PEIE) and poly [3-(6-trimethylammoniumhexyl) thiophene] (P3TMAHT), between the PCBM and Ag electrode which reduced the metal electrode work function and increased charge collection [42]. DMAPA-C_{60} based on an amine functionalized fullerene derivative was also used as CBL in perovskite which had PCE of 9.4% [36]. In 2014, Xue *et al.* reported PCE of 15% from 12.4% of control devices by using new amino-functionalized polymer, PN_4N as a CBL [43]. A solution-processed perylene–diimide (PDINO) was also used as a cathode buffer material that achieved PCE of 14%, reported J. Min *et al.* in 2015[44]. All the cases they have less efficiency compared to this work.

The optical properties of Polyvinylpyrrolidone (PVP) was reported by Thi *et al.* [45]. Later on, in 2016 Yunlong Guo reported PVP doped PSCs with PCE of 11.13% of best device condition [46]. In order to get high fill factor it was reported the common use of LiF and bathocuproine (BCP) as deposited on the top of the ETL [47, 48]. But, thermal vapor deposition was required which hindered the large scale PSCs production and made the fabrication complex.

In this work, a low cost, solution processed, non-conjugated PVP was reported, for the first time, as a material for CBL in perovskite solar cells between $PC_{60}BM$ and Ag electrode with a PCE of more than 16%.

1.3. Motivation

There is a need for developing low cost, solution processed and high performance PSCs considering CBLs engineering.

1.4 Objectives

The goal of this thesis was to use a conjugated polymer material as a CBL for PSCs with PCE more than 16% by controlling the CBL thickness and materials concentration and optimizing perovskite film formation.

To achieve the objective, the following tasks were performed:

1. Fabricate perovskite solar cell at different concentration of CBL material and layer thickness.
2. Study absorption of perovskite films fabricated at different CBL thickness using UV-VIS spectroscope.
3. Characterize the morphology and crystal structure of the perovskite films using atomic force microscope (AFM), XRD and Scanning Electron Microscope (SEM).
4. Measure transient photo current (TPC) and transient photo voltage (TPV) for charge transport time and carrier life time.
5. Fabricate and test PCE and external quantum efficiency (EQE) of perovskite solar cells with optimized perovskite crystal structure and morphology.

Chapter 2. Theory

2.1 Photovoltaics (PV): photon in and electron out

Photovoltaics is defined as a term which generates voltage and current in the presence of sunlight. More precisely, the conversion of light into electricity is called photovoltaics. The Sunlight is considered as radiation of photons or 'Packets' of energy at different wavelength. Photons cannot create electric carriers they can just excite the existing carriers. Interaction between an electromagnetic wave (or photons) and material is required to have a successful PV cell.

Photovoltaic effect is closely related to the photoelectric effect light matter interaction. Due to the incident light of different energy on a semiconductor material or PV cells, there will be emission of electron of corresponding wavelength of light.

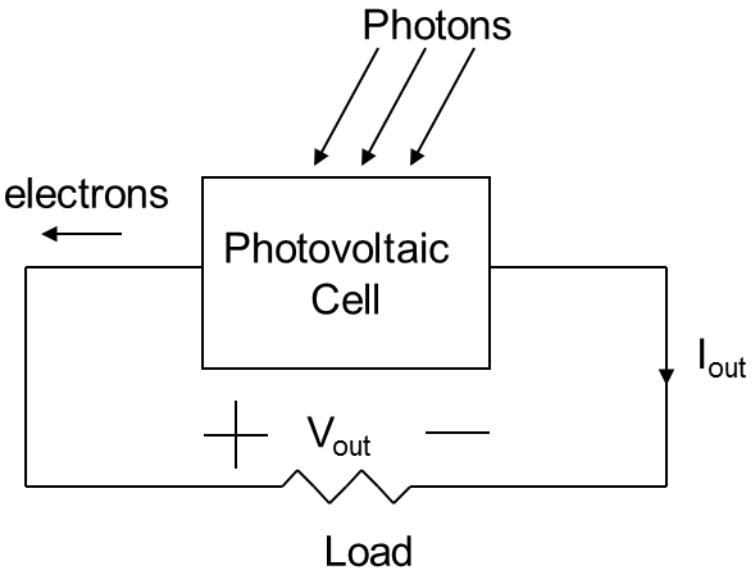

Figure 2. 1 Photovoltaic effect (Photon In, Electron in) [49]

If the velocity is c, the wavelength is λ and the frequency is ν of light, according to quantum theory of light, the energy of photon, E, is given by

$$E = h\nu = hc/\lambda \quad (2.1)$$

Where $h = 6.626068 \times 10^{-34}\ m^2Kgs^{-1}$ is called planks constant.

When photons incident on a semiconductor material the electron's from the ground state are excited to the higher energy states. In order to take place this phenomenon, the photon energy must have to be higher than the forbidden energy gap of that specific semiconductor material. It is so called absorption of photons. In photovoltaic devices, due to absorption process, a built in electric field is produced. However, excited electrons are extracted to the external circuit before they relax back to the ground state.

2.2 Photovoltaic material preference

The PV technology mostly use semiconductor materials for photovoltaic application due to their bandgap and availability of materials. Semiconductors have the conductivity in between an insulator and a conductor. According to the purity semiconductor can be classified as two types, one is intrinsic semiconductors which is highly pure with equal charges both negative and positive and another is extrinsic semiconductor which contains very minute quantities of impurities. The process of adding impurities is called 'Doping'. As intrinsic semiconductors are highly pure, it has high resistivity and less conductivity. To make it conductive it needs to be doped by some external impurities. Depending on the doping, there are two types of extrinsic semiconductors namely P-type and N-type semiconductor. In case of Si, a pentavalent dopant such as phosphorous are known as donor impurities since they donate one extra electron to the crystal structure hence it becomes N-type semiconductor. On the other hand a trivalent dopant such as boron that creates hole to the crystal structure and acts as P-type semiconductor.

2.3 P-N junction and solar cell

The p-n junction is nothing but a combination of p-type and n-type semiconductor. The modern PV cells are made of either crystalline Silicon or thin film semiconducting materials. The band gaps of semiconductors are generally in the range of 0.5-3 eV. Figure 2.2 shows absorption of light by the valence electron. Under light illumination, the valence electrons are excited to the conduction band and considered as a free electron and a free hole remains in the valence band.

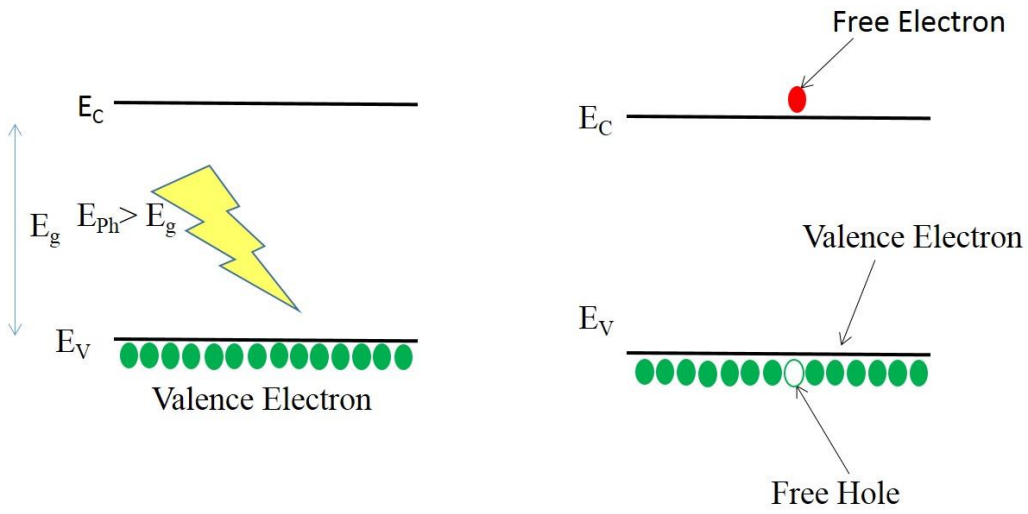

Figure 2. 2 Absorption mechanism and electron excitation from valence band to conduction band [49]

Silicon solar cell also works as the same principle of a p-n junction diode. Basically when the light falls in the junction, the photo absorber (p or n type depending on the structure) produces free charge of electron and hole which are collected through the respective electrodes in the presence of electric field. In practice the Si solar cell are not made in such a simple way of connecting p-type and n-type material but rather by diffusing a p-type dopant into one side of an n-type wafer or vice versa. Normally group III elements boron (B), aluminum (Al), gallium (Ga)) are used to dope for making p-type semiconductor

and group V elements phosphorous (P) and arsenic (As) are used to dope for making n-type semiconductor. Energy bandgap is a very important requirement for solar cell application. Crystalline Si has an energy band gap of 1.1 eV for corresponding wavelength of 1127 nm, so it can absorb all the wavelengths shorter than 1127 nm. There are some thermalization loss in photon absorbing interaction in semiconductor materials. For ideal case, 1.5 eV is considered an ideal energy band gap for solar cell application as it eliminates and keeps balance in both absorption and thermalization losses. Gallium Arsenide (GaAs) has an energy bandgap of 1.42 eV which provides excellent photovoltaic performance.

In p-type semiconductor, holes are the majority carriers and electrons are the minority carriers.

For p-type semiconductor, hole concentration (p) is written as

$$p = N_A \tag{2.2}$$

and electron concentration (n) can be found as

$$n = n_i^2 / N_A \tag{2.3}$$

For n-type semiconductor, electron concentration (n) is written as

$$n \approx N_D \tag{2.4}$$

and Hole concentration (p) can be found as

$$p = n_i^2 / N_D \tag{2.5}$$

Where n_i is the intrinsic carrier density, N_A and N_D are density of acceptors and donors.

Figure 2.3 shows energy band diagram of a p-n junction with the formation of space charge region (SCR). When incident light falls on the junction, the electrons excites from ground state to the excited state. Typically there are large number of free electrons in the n-side and very small number of electrons in the p-side. In case of holes it is vice versa. Due to

concentration gradient, there is diffusion of electrons from n-side to p-side and holes from p-side to n-side semiconductor material. The diffused electrons and holes recombine with each other near the junction and form a space charge region. In this region there exists both negative and positive charge carriers which are bound. This is also called the depletion region.

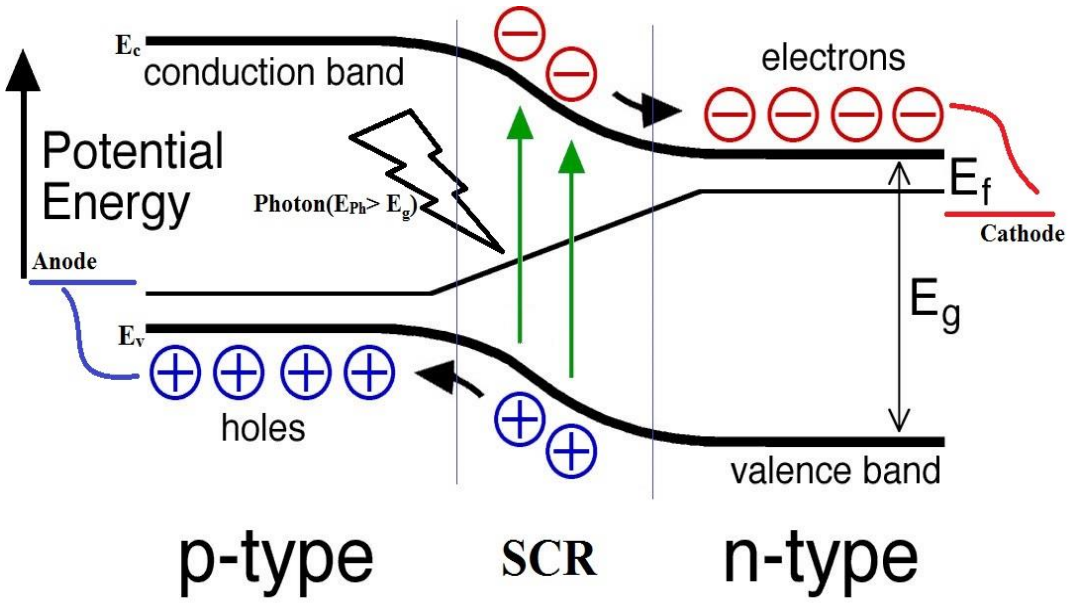

Figure 2. 3 Band diagram and carrier flow of p-n junction solar cell

The depletion region acts like a parallel plate capacitor which develops an electric field in the junction. The direction of electric field is from n-side to p-side. The built in electric field in the SCR region causes the flow of electrons and hole in the opposite direction. The conduction band and valence band are aligned according to the fermi energy levels of n-type and p-type semiconductor. The diffusion current density depends on the electron and hole concentration diffused from both sides and diffusion coefficient of n-type and p-type semiconductor materials.

If $J_{n,diff,}$ is the diffusion current density for electrons and $J_{p,diff,}$ is the diffusion current density for holes, it can be written as below

$$J_{n,diff} = qD_n \frac{dn(x)}{dx} \tag{2.6}$$

$$J_{p,diff} = -qD_p \frac{dn(x)}{dx} \tag{2.7}$$

where, D_n and D_p are diffusion coefficient of electrons and holes, n, p, and q are electron concentration, hole concentration and electron charge, respectively. The electric field V_{bi} in the SCR region carries the electrons and holes towards the cathode and anode. Thus, there is a depletion width, W in the p-n junction. It can be defined as follows.

$$W = \sqrt{\frac{2\varepsilon V_{bi}}{q}\left(\frac{1}{N_A} + \frac{1}{N_D}\right)} \tag{2.8}$$

where, ε is the dielectric permittivity of the semiconductor. The free electrons and holes will be diffused before recombination. Diffusion length is the average distance where the minority carriers can diffuse. The diffusion length for holes in n-type and for electrons in p-type is written as

$$L_p = \sqrt{D_p \tau_p} \tag{2.9}$$

$$L_n == \sqrt{D_n \tau_n} \tag{2.10}$$

where τ_n and τ_p are recombination lifetimes of electron and hole in p side and n side and D_n ,D_p have been defined in equations (2.6) and (2.7).

2.4 Electrical model of solar cell

A solar cell can be considered as an equivalent electrical circuit model. Figure 2.4 shows an electrical circuit model connected with current source, diode, series resistance (R_s) and shunt resistance (R_{sh}). The series resistance arises due to bulk resistance of semiconductor materials, bulk resistances of metallic contacts, interconnects etc and shunt resistance arises from the recombination of holes and electrons, foreign impurities and crystal defects.

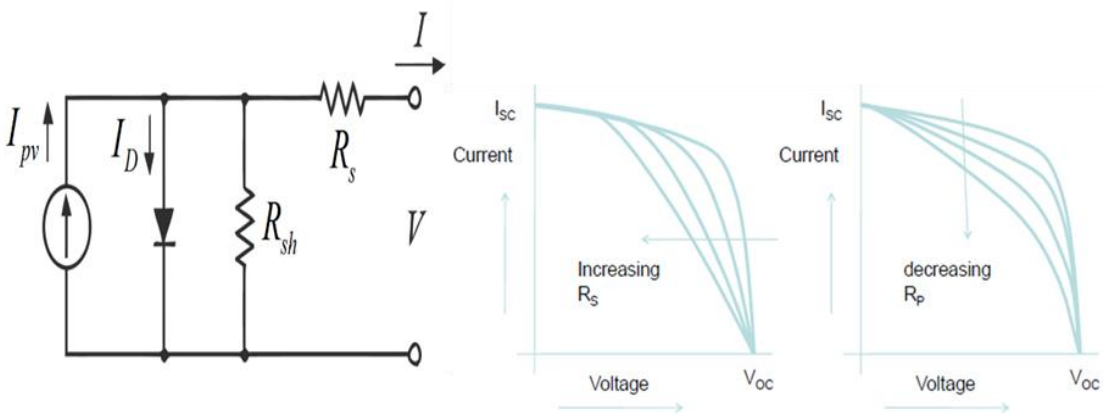

Figure 2. 4 Equivalent electrical model of solar cell and voltage-current characteristics for series (R_s) and shunt resistance (R_{sh}) [49]

The right side of the figure shows how the series and shunt resistances affect the I-V curve fill factor and the overall device performance. In ideal cases, R_s should be zero and R_{sh} should be infinite for high performances solar cell applications.

2.5 Solar cell performance determining parameters

2.5.1 Open circuit voltage

When there is no load connected with the external circuit, there will be no current flow, it is so called open circuit, and the voltage at that terminal is called open circuit voltage. It depends on photo-generated current density J_{PH} and is given by

$$V_{OC} = \frac{kT}{q}\left[\left(\frac{J_{PH}}{J_O}\right) + 1\right] \quad (2.11)$$

For organic solar cell, the difference between the highest occupied molecular orbital (HOMO) of donor electron and lowest unoccupied molecular orbital of acceptor electron is the open circuit voltage. For perovskite solar cell, figure 2.5 shows the measurement of V_{oc} and it can be written as

$$V_{OC} = \frac{1}{q}[E_{Fn} - E_{Fp}] \quad (2.12)$$

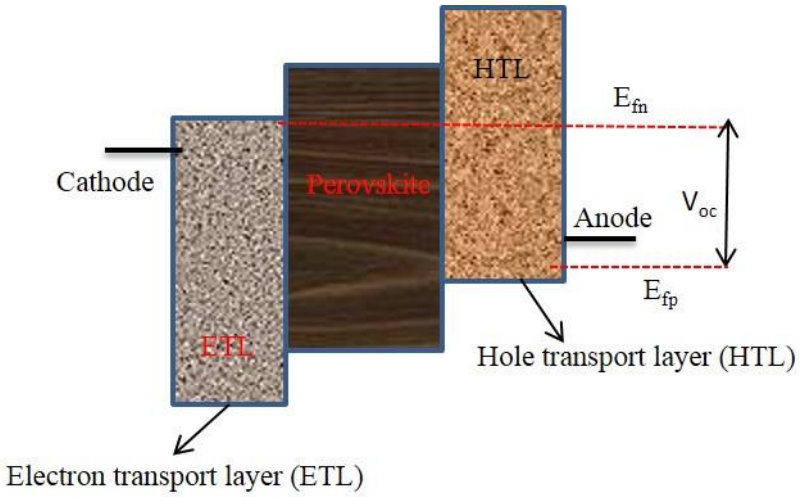

Figure 2. 5 perovskite energy band diagram for determining V_{oc}

2.5.2 Short circuit Current

When the voltage across the solar cell is zero, the current from the solar cell is termed as short circuit current, I_{sc}. For certain device area it is called short circuit current density (J_{sc}= I_{sc}/A). It also depends on light absorption, reflection, incident number of photons, light spectrum and charge collection probability of a solar cell. From figure 2.4, due to the external load connected with the solar cell, there is a voltage drop across the load that makes the diode forward bias. The direction of illuminated photo-current (J_{PH}) will be the opposite of diode current.

In dark condition, solar cells works like a diode. So the diode current equation is given by

$$J_D(V) = J_o\,(e^{qV/kT}-1) \qquad (2.13)$$

where, q is the electron charge, k is the Boltzmann constant and V is the voltage drop across the load at room temperature, T. The net current is written as

$$J = J_{SC} - J_o(e^{qv/kT}-1) \qquad (2.14)$$

where J_{sc} is the short circuit current when the voltage is zero. The short circuit current is shown in figure 2.6.

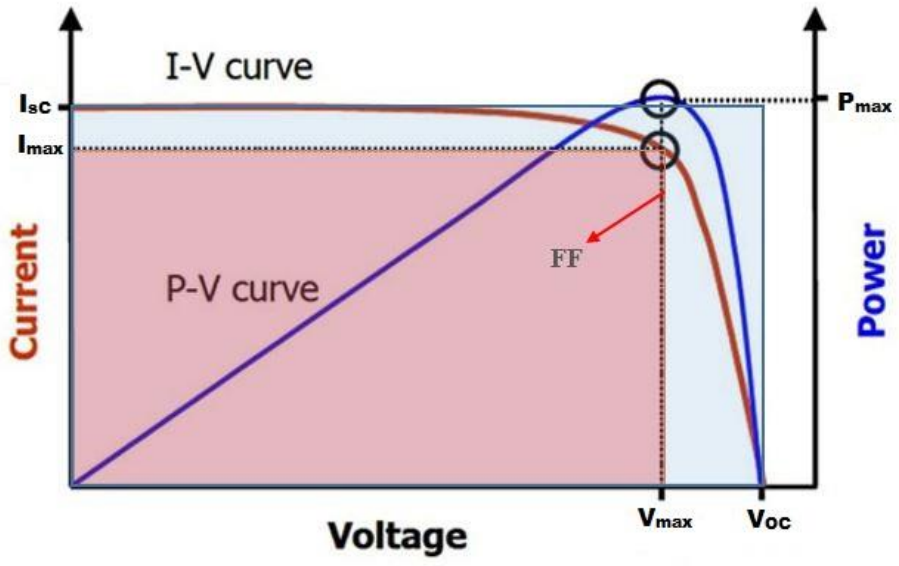

Figure 2. 6 I-V and P-V characteristics curve of a solar cell [49]

2.5.3 Fill Factor

The V_{oc} and J_{sc} are the maximum operating point of the solar cell. The fill factor (or FF) is the parameter that determines the maximum power from the solar cell. Mathematically, it is a ratio between the maximum power from the solar cell, P_{max} and the

product of V_{oc} and J_{sc}. Normally, it measures the squareness of the IV curve where the higher voltage has larger FF because the rounded portion of the IV curve takes up less area. The shaded area of figure 2.6 indicated the measuring fill factor

$$\text{FF} = \frac{P_{max}}{V_{OC} \times I_{SC}} = \frac{V_{max} \times I_{max}}{V_{OC} \times I_{SC}} \tag{2.15}$$

2.5.4 Power conversion efficiency (PCE)

The ratio of output energy to the input incident solar energy is defined is the power conversion efficiency. It depends on the incident of the light spectrum, intensity and other performance determining parameters of the solar cells. So, it determines the fraction of incident power which is converted to electricity and written as

$$\text{P}_{\text{max}} = FF \times V_{OC} \times I_{SC} \tag{2.16}$$

The efficiency of the solar cell is written as below

$$\text{Efficiency } (\eta) = \frac{P_{max}}{P_{in}} = \frac{V_{OC} \times I_{SC} \times FF}{V_{max} \times I_{max}} \tag{2.17}$$

2.5.5 External Quantum Efficiency (EQE)

The ratio of the number of electrons collected to the number of incident photons of a given solar cell is called the external quantum efficiency (EQE). It also depends on the intensity of incident light, solar spectrum, charge mobility and optical properties like absorption and reflection. It is written as

$$\text{EQE} = \frac{\text{Total number of electrons collected}}{\text{Total number of incident photons}} \tag{2.18}$$

J_{sc} can also be written as

$$\text{Jsc} = \text{q} \int EQE\ (E) \times \emptyset\ (E) dE \tag{2.19}$$

2.5.6 Internal Quantum Efficiency (IQE)

It is the ratio of number of charge collected to the number of photons absorbed in a given solar cell. It is expressed below

$$\text{IQE} = \frac{\text{Number of electrons collected}}{\text{Number of incident photons absorbed}} \tag{2.20}$$

2.6 Structure and properties of perovskite

In 1839, Russian mineralogist L. A Perovski first found a material called calcium titanate ($CaTiO_3$) and discovered the crystal structure of ABX_3 [50] which became known as perovskite structure.

2.6.1 Molecular structure

The molecular structure of perovskite is ABX_3 where A and B are the cations and X symbolizes the halide group as anions. There are lots of application of perovskite materials in transistor, light emitting diode, electronic devices and other energy transfer systems [51] [52] [53-55]. Most commonly used perovskite structure is shown in figure 2.7 where CH_3NH_3I (MAI) and lead (Pb) are cations and Iodine (I) is the halogenated atom which is anion. Perovskite absorber layer is the combination of MAI and PbI_2 where methylammonium iodide (CH3NH3I or MAI) is the organic part which facilitates self-assembly and lead iodide (PbI_2) is the inorganic salt which provides an extended network by covalent or ionic interaction that allows for precise crystalline structure formation. The electronic and optical properties are determined by the ratio of halide ions.

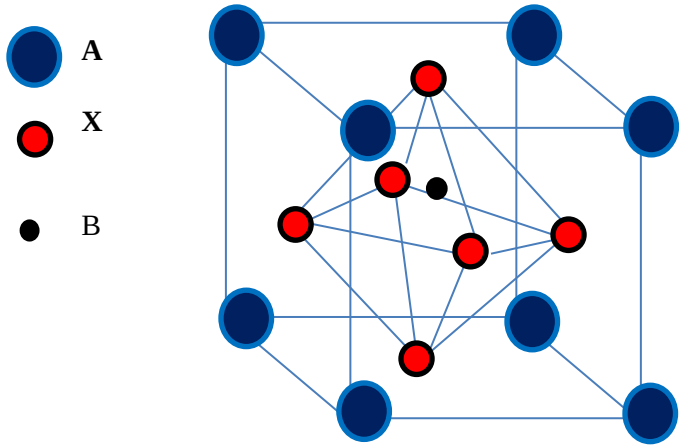

Figure 2. 7 Molecular arrangement of perovskite (ABX_3) [49]

2.6.2 Band gap tuning

The bandgap of perovskite can be tuned by the halide ions. The crystal orientation also changes according to their band gap position. The band gap can vary from 2.3 eV – 1.5 eV. Kulbak *et al.* showed the band of $MAPbBr_3$ perovskite absorber is around 2.32 eV where the bandgap of $MAPbI_3$ is around 1.5 eV [56]. This change of energy gap of perovskite absorber can be observed by cyclic voltammetry (CV), UV-Visible spectroscopy and EQE measurement tools.

2.7 Working principle of perovskite solar cell

2.7.1 Planar p-i-n structure

The elementary working assumption of PSC is when the sun light falls, the active perovskite absorber creates excitons which is the bound of both electrons and holes. According to the device structure, the active perovskite absorber is normally inserted between ETL and HTL. So the excitons are separated through ETL and HTL to the corresponding electrodes. In 2013, Samuel *et al.* demonstrated that excitons have weakly bound both free charges (electron and hole) that coexists within perovskite material [57]. The PSCs are grown on the fluorine doped tin oxide (FTO) or Indium doped tin oxide

(ITO) and the light is illuminated from the conductive glass side because the top electron is not transparent. A p-i-n structure based PSC is shown in figure 2.8. P-type hole transport layer, PEDOT: PSS is used bellow the perovskite and electron transport material PCBM is used on the top of the perovskite and metal electrode is connected through a buffer layer. The respective energy band diagram of p-i-n architecture perovskite solar cell is shown on the right side of figure 2.8. So the overall device structure is ITO/HTL/perovskite/ ETL/Ag which is also known as inverted structure of PSCs.

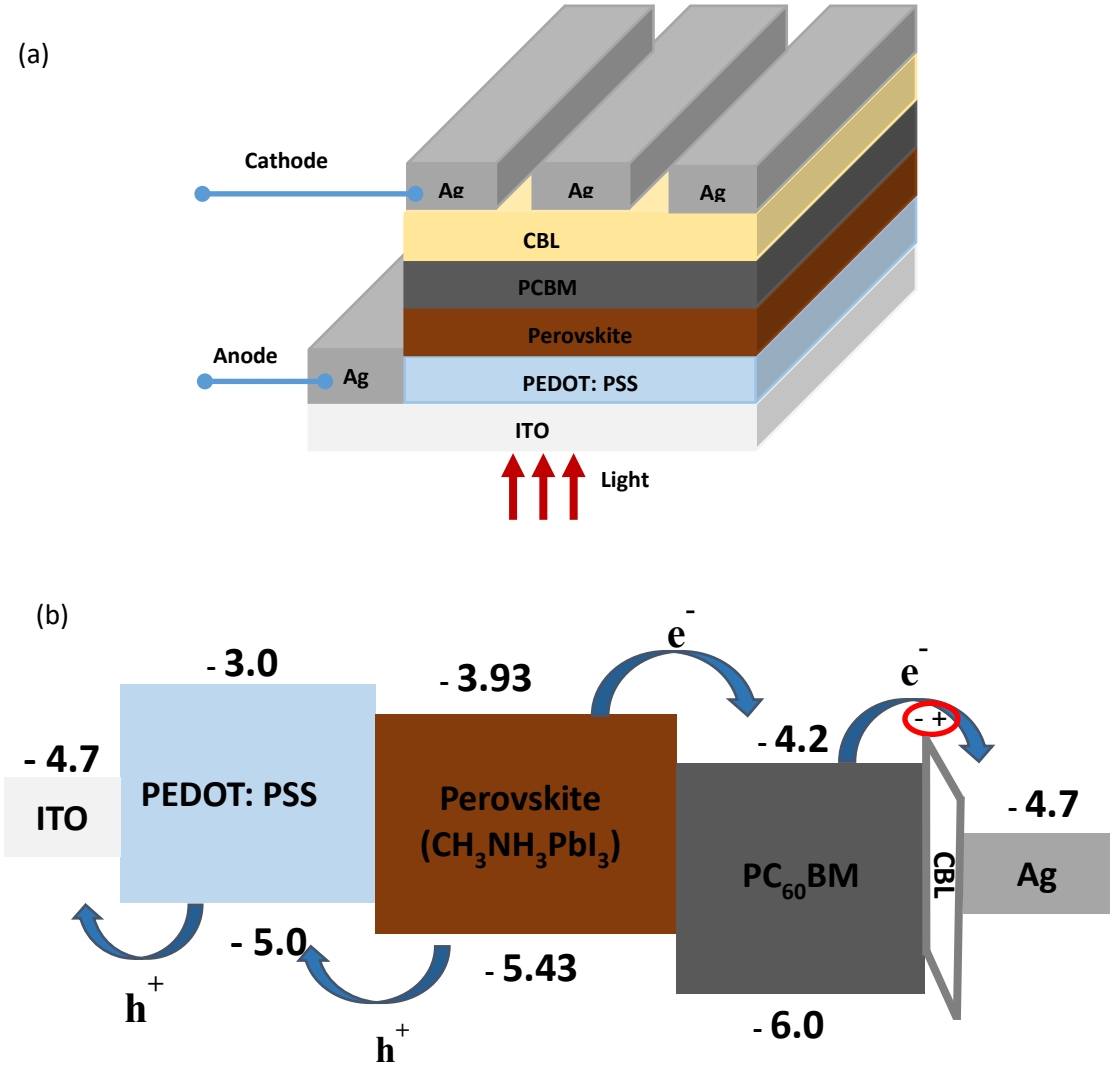

Figure 2. 8 Planar p-i-n PSCs (a) device structure (b) energy band diagram.

2.7.1 Planar n-i-p structure

The planar n-i-p structure PSC is totally opposite of planar p-i-n PSC. There are several electron transport layers commonly used including titanium dioxide (TiO_2), copper thiocyanate (CuSCN), zinc oxide (ZnO) nanorod, and PCBM and the hole transport layers are used including polymer, spiro-MeOTAD, and PEDOT: PSS. The planar n-i-p structure perovskite solar cell and its energy band diagram are shown in figure 2.9. Mostly used TiO_2 used ETL is deposited on FTO and spiro-MeOTAD is used to cap the active perovskite layer. So the overall device structure is FTO/ETL/perovskite/ HTL/Ag which is also known as regular structure of PSC.

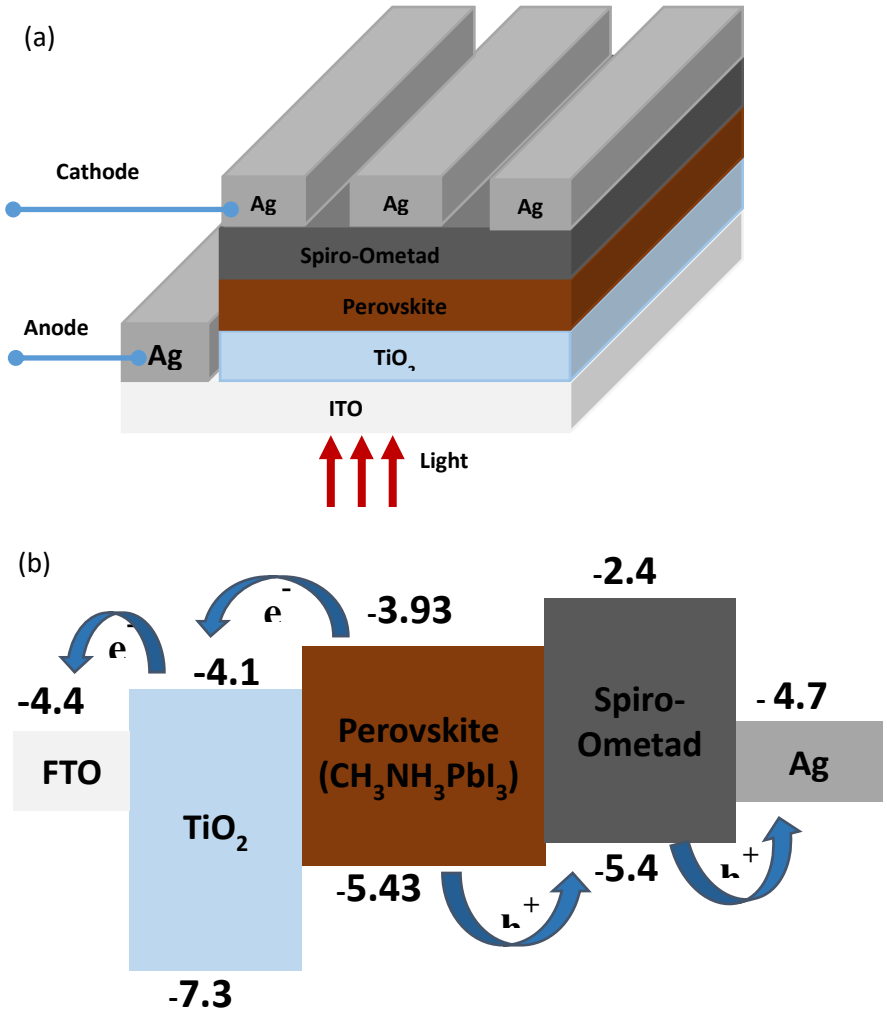

Figure 2. 9 Mesoscopic scaffold n-i-p PSCs (a) device structure (b) energy band diagram.

2.8 Electrode buffer layer and charge transport materials

2.8.1 Electron transfer and buffer layer

There are some metal oxides that can be used as electron transport material and buffer layer as well.

a) TiO_x: Mostly used TiO_x has promising electronic band structure, photoelectric properties and chemically stable to be preferred for electron transfer materials. In solar cell application, two different crystal structure rutile and anatase are used. Anatase structure is used widely in DSSC due to its better photocatalytic activity. The conduction band of TiO_x is around -4.4 eV which matches with the fullerene derivatives (-4.0 eV~ -4.3 eV). X. Bao *et al.* reported about compact TiO_x which has good transparency and acts as antireflective in some range of wavelength [58]. Yella *et al.* reported rutile TiO_x nanoparticle structure for perovskite solar cell by using thermal annealing aqueous $TiCl_4$ solution which control the size of TiO_x nanoparticles [59]. Besides TiO_x nano-sheet, TiO_x nano-rods, nanofibers have also been used in solar cell as an electron transport layer [30, 60, 61].
b) ZnO: The band gap of transparent ZnO is 3.7 eV and has better optoelectronic properties and high electron mobility. Like TiOx, ZnO is also n-type metal oxides. The highest occupied molecular orbital (HOMO) is -7.6 eV and lowest unoccupied molecular orbital (LUMO) is -4.4 eV respectively [62]. ZnO has been widely used in organic and perovskite solar cell as ETL. ZnO nanorod film is used as ETL and scaffold for the deposition of perovskite material. If ZnO compact film is used in the top of ITO,

it acts as hole blocking layer that prevents recombination process of electrons and holes.

c) Graphene: As a two dimensional material structure, graphene offers very high electric conductivity and mobility. Due to excellent conductivity, graphene has been used widely in photovoltaic, supercapacitor, electrodes, etc. [63-65]. Both graphene and TiO_x are formed as combine graphene/TiO_x nanoparticles which significantly increases the electrical conductivity. Compared to the LUMO level, both graphene and TiO_x are similar. Wang stated novel low temperature processed graphene/TiO_x as ETL layer for solar cell application [66].

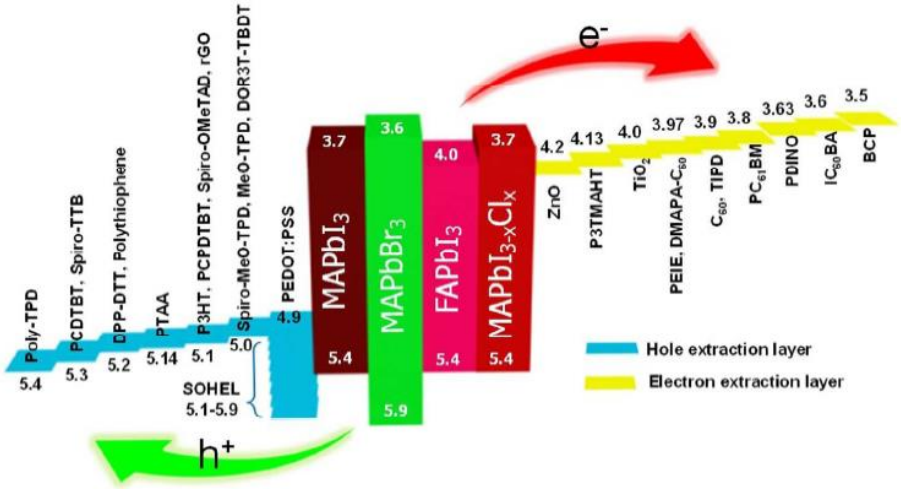

Figure 2. 10 Energy level diagram of HELs (left) and EELs (right) used in perovskite light absorbers [67]

d) Fullerene derivatives: Fullerene derivatives are one of the best choice for p-i-n structure based PSCs as a good ETL due the large electron affinity of C_{60}. Basically, C_{60}, phenyl-C_{61}-butyric acid methyl ester ($PC_{61}BM$), and phenyl-C_{71}-butyric acid methyl ester ($PC_{71}BM$) all are used as transport layer (ETL). Some researchers have used $PC_{71}BM$ as ETL. Jeng reported PSC devices with three different fullerene derivative: C_{60},

$PC_{61}BM$ and indene-C_{60} bisadduct (ICBA) but they found that $PC_{61}BM$ as ETL based devices showed higher performance compared to C_{60}.

2.8.2 Hole transfer and buffer layer

a) Spiro-OMeTAD: Most commonly used hole transfer material named 2, 2', 7, 7'-tetrakis (N.N-di-p-methoxyphenylamine)-9-9'-23 spirobifluorene or simply spiro-OMeTAD was first used in DSSC by replacing organic electrolyte. The HOMO level of spiro-OMeTAD is -5.22 eV which is more preferable for PSCs. Spiro-OMeTAD was first used in perovskite by Kim [68, 69].

b) PEDOT: PSS: It is a polythiophene based conjugated polymer mixture of two ionomers. PSS are part of sulfonyl group that carries negative charges and the other component PEDOT is a conjugated polymer that carries positive charges. PEDOT: PSS is water-soluble and highly conductive polymer. Zhou *et al.* first reported PEDOT: PSS based solar cell as electrode and achieved PCE 0.7% [70]. Later on it was optimized the thickness of PEDOT: PSS layer and obtained better PCE. Now, PEDOT: PSS is widely used in PSC as HTL.

c) P-type low band gap polymer: The conjugated polymers whose energy band gap is lower than 2 eV is considered as low bandgap polymer. Typically, conjugated polymer has π-delocalized structure in its backbone from where charges can easily transfer through the entire backbone and gives higher carrier mobility [71, 72]. Low band gap conjugated polymers are widely used in organic light emitting diode and PSCs even as buffer layer.

d) MoO_3: As a metal oxide, MoO_3 can also be used as HTL in PSC. In 1990, Tokito et al. reported MoO_3 as HTL in organic photovoltaics [73]. Several transition metal oxide

such as V_2O_5, MoO_3, RuO_2 have been reported by scholar [73]. The improvement of hole injection has been observed when using the above metal oxide as HTL in organic light emitting diode [74]. Transition metal oxides have been used widely because of its high work function, decent transparency and semiconducting properties [75]. The LUMO and HOMO level of MoO_3 has -2.3 eV and -5.3 eV, which is well-matched to the HOMO level of perovskite which is -5.3 eV. Liu reported MoO_3 as CBL in OPV [76].

2.9 Device characterization technique

2.9.1 UV-vis spectroscopy

Ultraviolet-visible or shortly UV-Vis spectroscopy is typically an absorption spectroscopy or reflectance spectroscopy that investigates the light absorption or transmission in the range of ultraviolet, visible and near infrared of electromagnetic spectrum. Figure 2.11 shows the light absorption and transmission mechanism of UV-Vis spectroscopy. When the light falls on a material or liquid solution or thin film, it may be reflected or absorbed and transmitted by the material or liquid solution or the thin film. The light will be absorbed if the electron goes to excited state from its ground state. The UV-Vis spectroscopy consists of deuterium arc lamp and tungsten lamp as light source that can generate 280 – 1100 nm wavelength of light, a monochromator and a detector which detects the materials properties. The thickness of absorbing material determines the amount of light that will be absorbed. It is also used to determine absorption coefficient, refractive index and dielectric constant of a material.

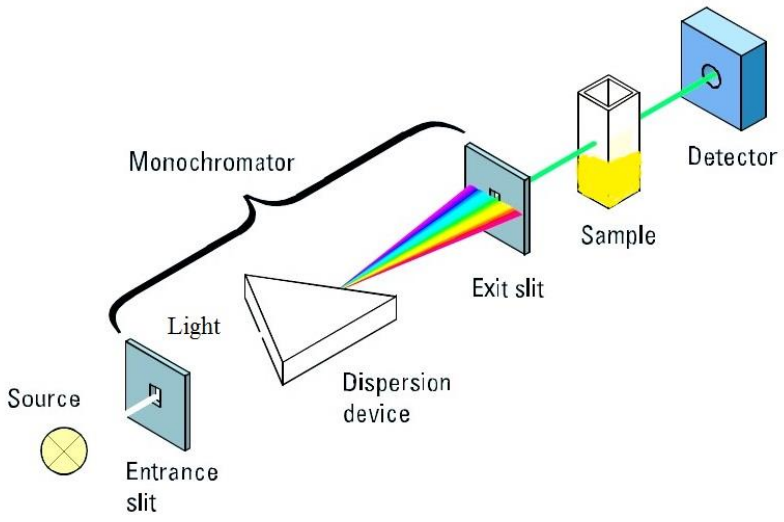

Figure 2. 11 Schematic principle of UV-Vis spectroscopy

According to the Beers Lambert law, the principle of UV-Vis absorption spectroscopy is written as.

$$\text{Absorbance (A)} = -10Log_{10}(\frac{I}{I_o}) = \epsilon bc \tag{2.21}$$

where I_0 is the intensity of light before passing the sample with thickness d, I is the intensity of light after passing the sample. ϵ, b, c are molar extinction coefficient, path length of the sample holder and concentration of the dissolved molecule.

2.9.2 X-ray diffraction

X-ray diffraction (XRD) is a measurement technique for measuring the atomic and molecular structure of perovskite specimen. It can also investigate composition of sample, phase, lattice spacing, residual strain, Bravais lattice symmetry, relative crystallinity and lattice orientation in the measured sample. The XRD instrument basically consists of four parts (1) X-ray source, (2) goniometer, (3) sample holder, and (4) detector. X-ray source is a monochromatic X-ray beam itself. The goniometer is used to position the crystal at selected orientations. The sample and detector are rotated to adjust the proper angle of X-

rays diffracted by the sample and detected. Figure 2.10 demonstrates the working principle of XRD measurement. The measurement can be taken in-plane or out of plane. In-plane XRD measurement technique is developed for measuring diffraction intensities from lattice planes perpendicular to the surface of a sample and out of plane measurement technique is almost parallel to the sample. Out of plane measurement is chosen for perovskite thin film samples.

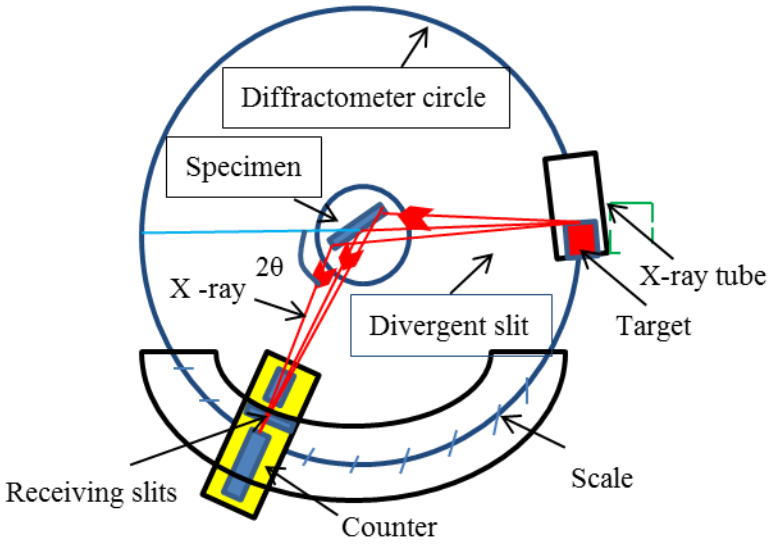

Figure 2. 12 Schematic diagram of XRD

Bragg's law explains the diffraction principle of XRD. Diffraction occurs when the incident X-ray beam is comparable to atomic spacing and it is scattered by the atoms of crystalline system and causes constructive interference.

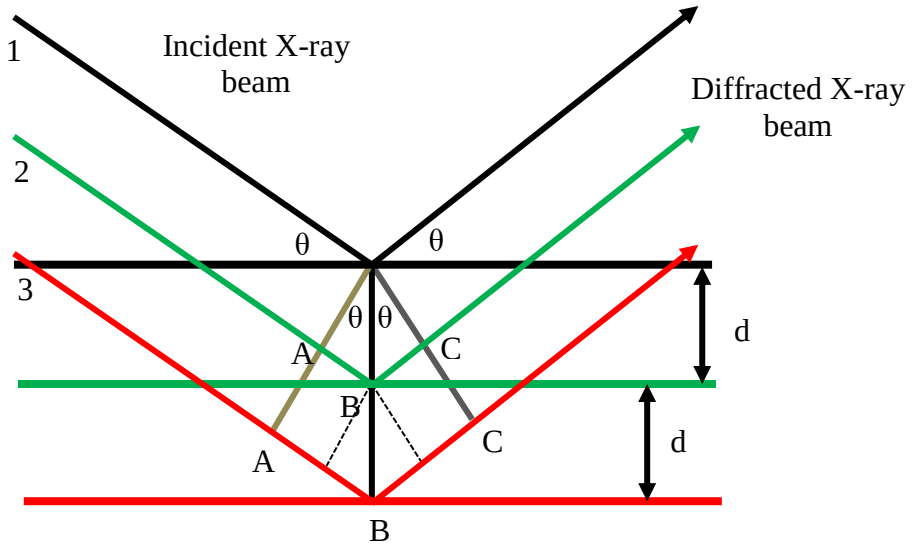

Figure 2. 13 Braggs law of diffraction

According to the Bragg's law of diffraction, when the path difference between the two angles of incident X-rays and the rays reflected back at different planes is equal to integral (n) multiple of wavelength (λ) then the interference will be constructive otherwise it will cause destructive interference. So for constructive interference it can be written as

$$2d\sin\theta = n\lambda \qquad (2.22)$$

where, 2dsinθ is the path difference, d is the spacing between the crystal layer, λ is the wavelength of the X-ray, n is the integer number, θ is the incident angle and reflected angle. For a cubic lattice, lattice constant, d, is written as

$$d = \frac{1}{\sqrt{h^2+k^2+l^2}} \qquad (2.23)$$

Where, h. k and l are lattice parameters.

2.9.3 Atomic force microscope (AFM)

It is very important for the device to measure its local, electrical and magnetic properties, such as height, friction, surface potential and magnetism. Scanning probe

microscope (SPM) is the better choice to deal with this measurement. The atomic force microscope (AFM) is a form of SPMs which has resolution more than 1000 times higher than the optical diffraction limit. It determines the force between a probe and the sample. Atomic force microscope (AFM) is a type of high resolution scanning probe microscope.

AFM consists of four basic components: (1) cantilever with a sharp tip is used to scan the sample surface. It is typically made of silicon or silicon nitride in the range of nanometer with curvature tip radius. (2) A photodiode which determines the deflection of cantilever. An array of position sensitive photo detector (PSPD) is used to detect the deflection. The reflected laser beam is detected by a PSPD which is segmented into four quadrants. (3) Laser and (4) a scanner which scans the specimen surface. Figure 2.14 shows the schematic of an atomic force microscope and its working direction. As AFM is concern about the force in the cantilever tip, it leads to deflection according to Hooke's law. The AFM measurement includes mechanical contact force, Vander Walls force, magnetic force, capillaries force and so on.

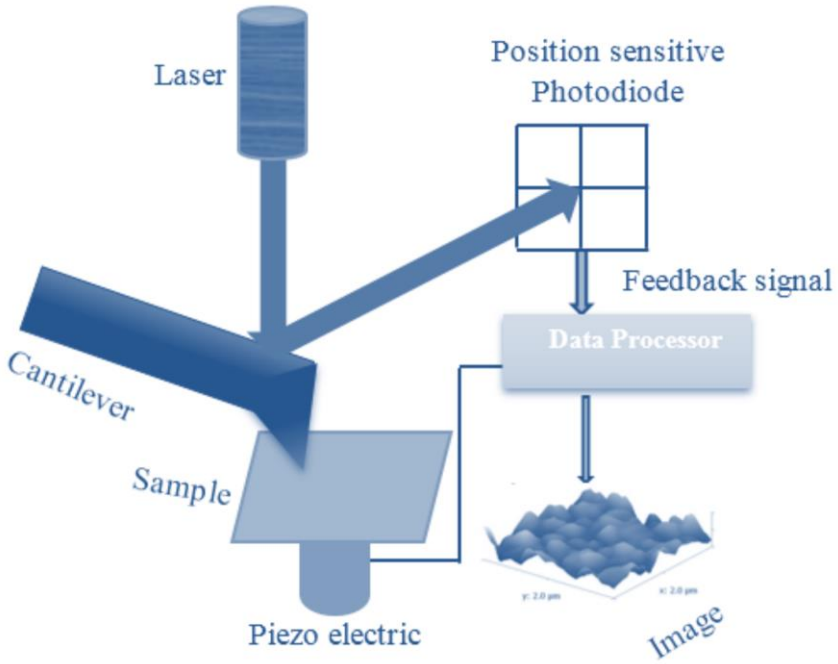

Figure 2. 14 Schematic of an atomic force microscope [49]

AFM measurement can be taken in 3 different modes: (i) tapping or intermittent AC mode, (ii) contact mode and (iii) non-contact AC mode. These modes determine the surface topographical information of the sample, specially domain formation, surface roughness, surface orientation and height of the particles. When the tip goes close to the sample, attraction force is generated as shown in figure 2.15. The attraction force increases with the decrease of distance between the tip and the sample. After certain distance, the attraction force becomes zero. The separation approaches to a couple of angstroms. Beyond this distance, another force becomes active that is called repulsive force. In this condition, the cantilever bends and the cantilever drives the tip to take it away from the sample rather than driving the tip closer to sample atoms.

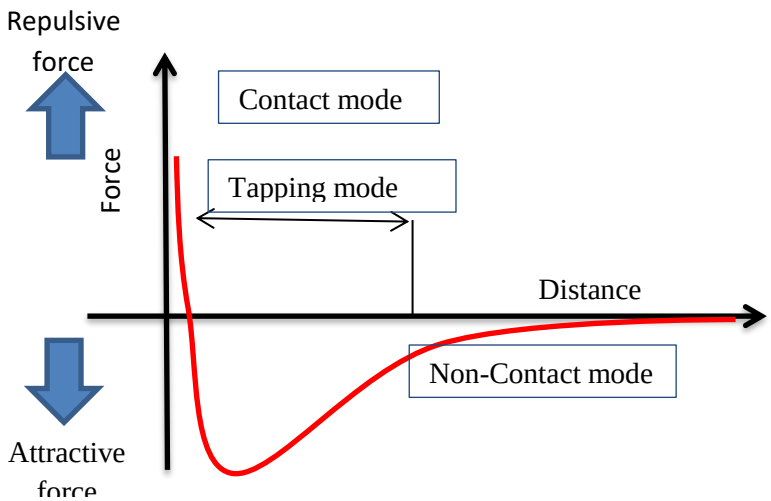

Figure 2. 15 Different modes of AFM with respect to force

Tapping mode is used to find the phase images of the sample and provides information about materials composition, adhesion and viscoelastic properties of specimen. Contact mode is used to measure the current sensing by dragging the tip through the surface of the test specimen. The outlines of the surface are measured from the deflection of the cantilever which requires necessary feedback signal to keep it at a constant position. Non-contact mode is used to measure soft samples like biological samples or organic thin films. During measurement, cantilever does not contact with the sample surface. The cantilever vibrates its resonant frequency or just little above, where the amplitude of vibration is basically a few nanometers (<10 nm) down to a few pico-meters.

2.9.4 Kelvin probe force microscope (KPFM)

In 1898, Lord Kelvin first developed a technique for the measurement of surface potentials [77]. According to his name it is called kelvin probe force microscopy (KPFM). It is also familiar as surface potential microscopy (SPM) that works on non-contact mode of Atomic Force Microscopy (AFM). It determines the local surface potential of a sample

with high spatial resolution. Non-contact basically minimizes the electrostatic interaction between tip and sample. The work function of surfaces can be measured at atomic or molecular scales with KPFM by either amplitude modulation or frequency modulation technique. This measurement is considered like a parallel plate capacitor where contact potential difference (CPD) is generated. The measured sample acts as one of the plate and probe i.e., tip with known work function acts as another plate of the capacitor. The capacitance changes with the vibrating of the probe or tip at frequency, w, and results in alternating current in the plates. A dc-voltage is applied either the tip or the sample to minimize this current to zero. This voltage is the contact potential difference (CPD) of the two materials. This contact potential difference can be measured by applying an external dc bias in opposite direction of CPD where external dc bias nullifies the contact potential difference.

Mathematically, the contact potential difference, V_{CPD} between AFM tip and sample is expressed as [78]

$$V_{CPD} = \frac{\emptyset_t - \emptyset_s}{-e} \tag{2.24}$$

Where ϕ_t and ϕ_s are work functions of AFM tip and sample respectively. Figure 2.16 shows the block diagram of kelvin probe microscope where it uses two lock in amplifiers.

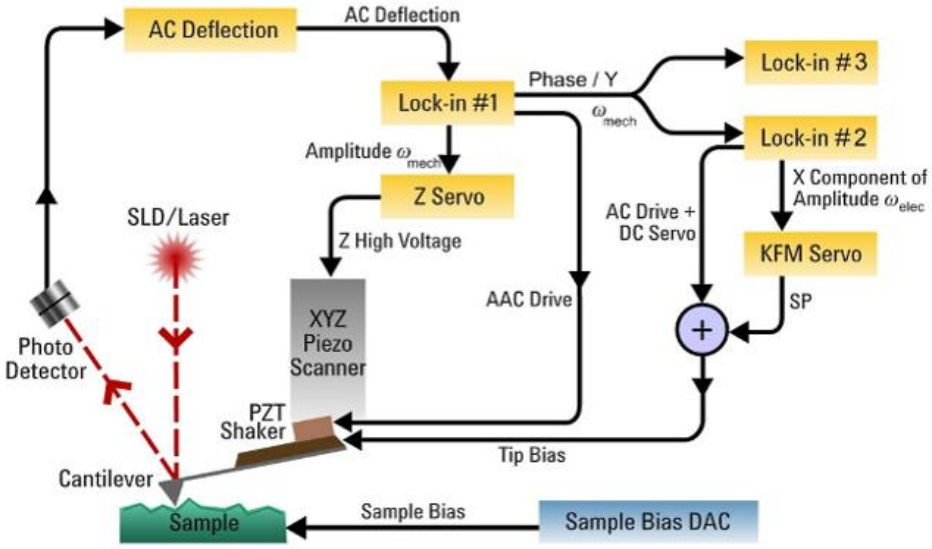

Figure 2. 16 Block diagram of Kelvin probe force microscopy (KPFM) [79]

Lock-in-amplifier number 1 vibrates the AFM cantilever at mechanical resonance frequency. Lock-in-amplifier number 2, applies a DC and AC electrical bias to the conductive AFM tip that induces an electrostatic force (F_c) between tip and sample. It can be written as

$$F_c = \frac{1}{2}\left(V_{tip} - \phi_{CPD}\right)^2 \frac{dC}{dZ} \tag{2.25}$$

$$V_{tip} = V_{dc} + V_{ac} \sin(\omega_{elec} t) \tag{2.26}$$

Where, ω_{elec} is the frequency of AC bias applied to the tip and V_{dc} is the dc bias applied to the tip, C is the capacitance and ϕ_{CPD} is the contact potential difference between the tip and sample.

2.9.4 Scanning electron microscope (SEM)

Scanning electron microscope (SEM) produces the images of a sample by scanning its surface with a focused electron beam. The electron beam interacts with atoms in the measured sample and produces various signals such as secondary electrons, backscattered electrons, diffracted backscattered electrons, photons, visible light and heat. The secondary electrons and backscattered electrons have information about the test specimens surface morphology and topography. Figure 2.17 shows the schematic of scanning electron microscope which describes the working principle.

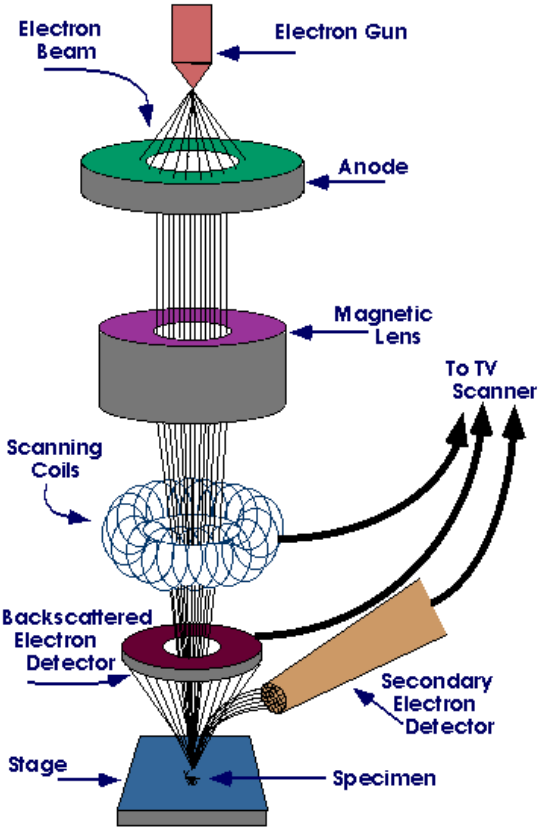

Figure 2. 17 Schematic of Scanning electron microscope [49]

The electron beam is created from an electron gun which is cathode and then it is accelerated by anode. The diameter of accelerated electron beam is then confined by the

magnetic condenser lenses. Scanning coil creates a magnetic field that confines the electron beam backward and forward. The electron beam is further highly confined by objective lens on the sample to scan the surfaces. The primary electrons hit the sample surface which emits secondary electrons which is detected and viewed as a photographic image in the computer. As wavelength of an electron beam in an SEM is much lower than wavelength of visible light, SEM can achieve resolution better than 1 nanometer.

2.9.5 Transient photo voltage and photo current spectroscopy

Transient photo voltage (TPV) and photo current (TPC) are a measurement technique to study the time-dependent extraction of charges (charge carrier lifetime and charge transport time) generated by photovoltaic effect in semiconductor devices. The device efficiency will reduce if recombination takes place. So it is important to sweep out charges to the electrodes to reduce recombination loss at earliest convenience. The transient measurements depends upon the resistor capacitor (RC) time constant of the device which is observed in oscilloscope. In TPV measurement the solar cell device is connected at open circuit condition (i.e. using high impedance of oscilloscope 1MΩ) with a small short-lived laser pulse under light illumination and steady state conditions. The intensity of light illumination can be varied. The lifetime of the charge carrier in the device is calculated using mono exponential fitting that depends on RC time constant of solar device. Figure 2. 18 shows the schematic of TPV where its decay curve obtained through 1MΩ resistance of oscilloscope. The voltage decay in TPV is written as

$$\Delta V = \Delta Vo \times \exp(\frac{-t}{\tau}) \qquad (2.27)$$

Where τ is the charge carrier life time.

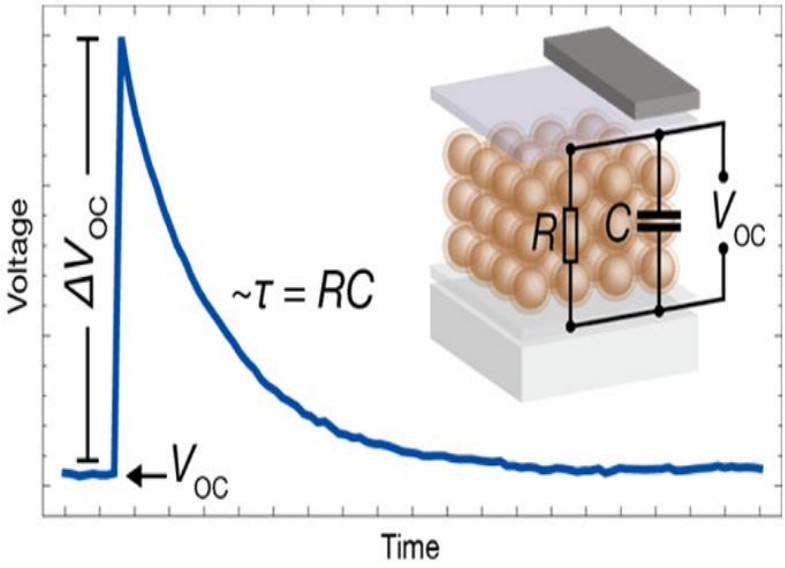

Figure 2. 18 Transient photovoltage measurement [80]

In TPC measurement the solar cell device is connected at short circuit condition (i.e. using low impedance of oscilloscope 50 Ω) with a small short-lived laser pulse under steady state conditions.

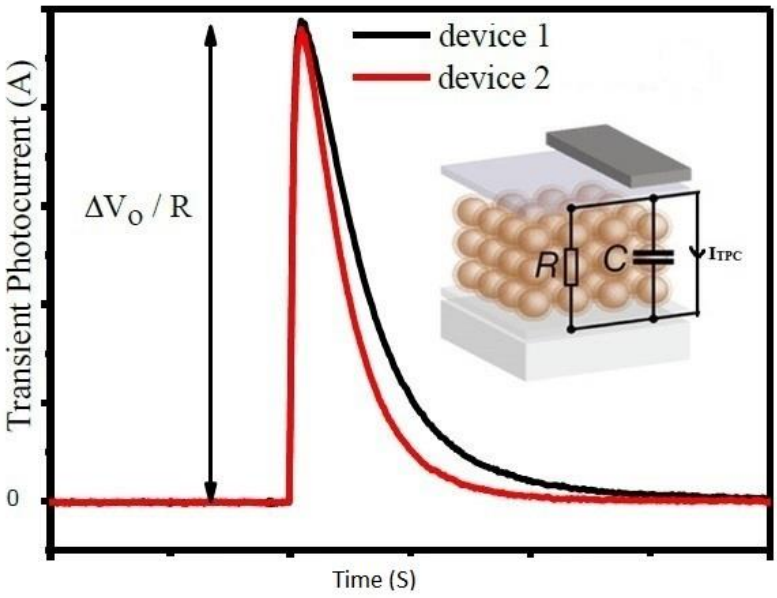

Figure 2. 19 Transient photocurrent measurement [80]

The charge transport time of the solar device is calculated using mono exponential fitting that depends on RC time constant of that solar device. Figure 2. 19 shows the schematic of TPC where its decay curve obtained through 50 Ω resistance of oscilloscope. The voltage decay in TPC is written as

$$\Delta I = \Delta Io \times \exp(\frac{-t}{\tau}) \quad (2.28)$$

The value of ΔI_o is found using $\Delta I_O = \frac{\Delta Vo}{R}$

where τ is the charge transport time of solar device.

Chapter 3. Experimental Procedures

3.1 Materials:

Methylammonium iodide (CH_3NH_3I) was purchased from Dyesol. PbI_2 (99%) was ordered from Acros organics. Anhydrous dimethyl sulfoxide (DMSO) (> 99.9%) and γ-butyrolactone (>99%) were obtained from Sigma Aldrich. Clevios™ P VP AI 4083 PEDOT: PSS was received from Heraeus. $PC_{60}BM$ and Rhodamine were purchased from Nano-C and Sigma Aldrich, respectively. Polyvinylpyrrolidone (PVP) powder with molecular weight of 40,000 was ordered from Alfa Aesar (USA).

Table 3. 1 Materials used for fabrication of perovskite solar cell

Layer	Material
Anode	Indium tin oxide (ITO)
Hole transport layer (HTL)	PEDOT:PSS
Active layer	Perovsktie ($CH_3NH_3PbI_3$)
Electron transport layer (ETL)	$PC_{60}BM$
Cathode buffer layer (CBL)	Polyvinylpyrrolidone or Rhodamine
Cathode	Silver (Ag)

3.2 Substrate cleaning:

Indium tin oxide (ITO) substrates were used to fabricate perovskite solar cell. Before fabrication it was required to clean the substrate properly. Transparent and conductive indium tin oxide (ITO) coated glass substrates were numbered and positioned in a Teflon sample holder. The sample holder was dipped in a beaker with soap (Sodium dodecyl sulfate) mixed DI water and ultrasonically cleaned for 20 minutes. Figure 3.1 shows a photograph of ultra-sonicator (FS30H) used for ITO substrate cleaning. After that

the substrates were cleaned sequentially with deionized water, acetone and isopropanol solvents for 20 minutes each.

Figure 3. 1 Photograph of Ultra-sonicator used for cleaning substrates

3.3 Device fabrication

The planar p-i-n structure based perovskite solar cells were fabricated using indium tin oxide (ITO) as bottom electrode, PEDOT:PSS as hole transport layer (HTL), light absorbing perovskite layer, $PC_{60}BM$ as electron transport layer (ETL), Polyvinylpyrrolidone or Rhodamine as thin CBL and silver (Ag) as top metal electrode [81]. After cleaning the substrates by ultra-sonicator with sequential steps followed, substrates were dried out in a flow of nitrogen gas and positioned into RF surface plasma cleaner (PDC-32G). Plasma cleaner was placed into low vacuum (10^{-2} Torr) and was purged with oxygen gas after 5 minutes. Then the RF coils were given medium power to generate a purple colored oxygen plasma. After 25 minutes of oxygen plasma cleaning the chamber was vented with air to remove the plasma cleaned samples. Figure 3.2 shows a photograph of plasma cleaner used for surface treatment of substrate.

Figure 3. 2 Photograph of plasma cleaner for cleaning substrate.

The plasma treated substrates were placed in the spin coater for PEDOT: PSS layer. The spin coating speed was 4500 rpm for 1 minute and immediately transferred on hot plat for annealing in air at 150 ºC for 10 minutes. After cooling down, the samples were then transferred inside a N_2 filled glove box for perovskite layer. A 581 mg of PbI_2 (1.26 M) and 209 mg of CH_3NH_3I (1.3 M) were mixed together in 1 ml of γ-butyrolactone: DMSO in 7:3 volume ratio and stirred overnight at 70ºC. Perovskite solution of 750 µL was spin coated for two step rpm, first at 750 rpm for 20 sec and then 4000 rpm for 60 sec. After 40 sec of total spinning time, 160 µl toluene was dropped. The films were then crystallized by thermal annealing at 80 ºC for 20 minutes for perovskite crystallization. Figure 3.3 shows spin coating procedures of different layers.

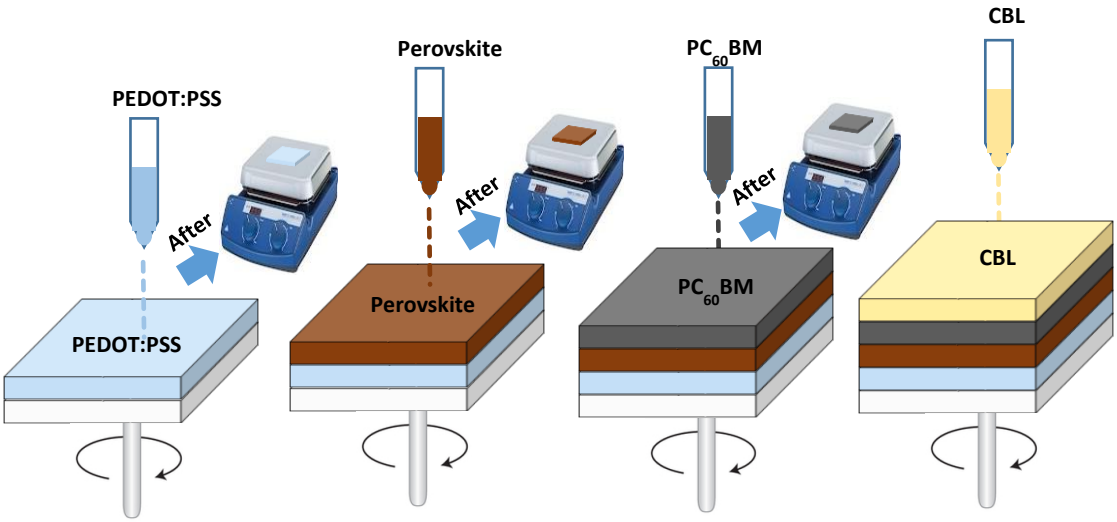

Figure 3. 3 Fabrication procedure of procedure of different layers

$PC_{60}BM$ solution was prepared in dissolving chlorobenzene (20 mg/ml) and then spin coated on top of the perovskite layer at 2000 rpm for 40 sec and then kept for 5 minutes inside the glove box for solvent drying at ambient temperature. Polyvinylpyrrolidone (PVP) was dissolved in isopropyl alcohol at different concentration (0.5, 1.0, 1.5 and 2.0 mg/ml) and then spin coated (1000, 3000, 5000 rpm) as CBL on the top of $PC_{60}BM$ layer. Few $PC_{60}BM$ coated films were spin coated using Rhodamine (0.5 mg/ml in isopropyl alcohol) as CBL at 3000 rpm for 40 sec. Finally Ag (80 nm) electrode was then deposited using thermal evaporation in high vacuum of 2×10^{-6} mbar. The area of shadow mask 0.16 cm^2 was considered for solar cell active area.

3.4 Optoelectronic characterization

3.3.1 Current density vs voltage (J-V) measurements

J-V measurements were accomplished using Agilent 4155C semiconductor parameter analyzer and xenon lamp (Newport 67005) with AM 1.5 filter as solar simulator. A calibrated silicon photo detector provided by National Renewable Energy Laboratory

(NREL) (Hamamatsu S1133-14) was used as reference cell to calibrate the light source to maintain the intensity of 100 $mWcm^{-2}$. The distance between the xenon arc lamp and the silicon detector was maintained to give A.M 1.5 illumination on the sample surface. After that, the photo detector was substituted by a perovskite solar cell at same position. Data was picked up from semiconductor parameter analyzer. Voltage was varied from 0 to1.1 V with an interval of 10 mV. Figures 3.4 and 3.5 show the setup for I-V measurements.

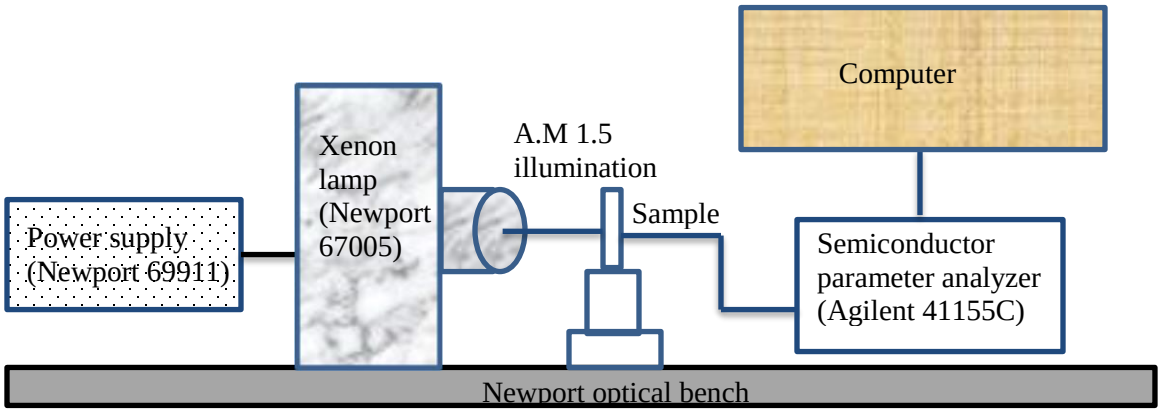

Figure 3. 4 Schematic of current density-voltage measurement system.

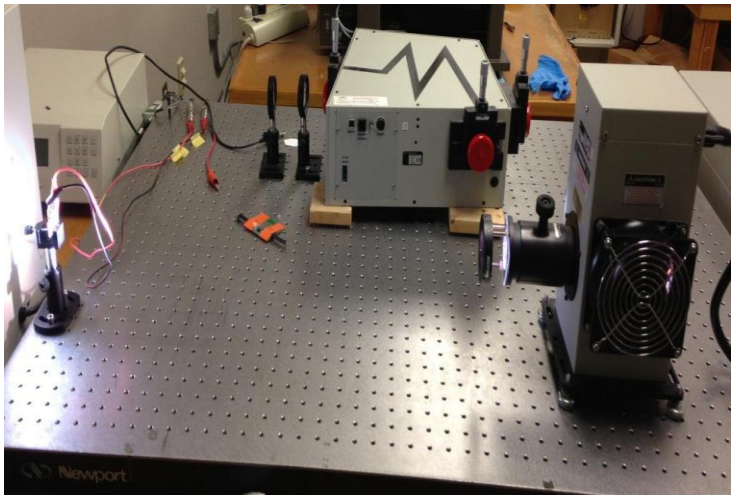

Figure 3. 5 Photograph of an experimental arrangement for I-V measurement set up

3.3.2 External quantum efficiency (EQE) measurement

Figure 3.6 show an experimental set up for EQE measurement. EQE measurement was carried out using a Newport EQE measurement kit with a 7412 Oriel Cornerstone 260 ¼ m monochromator in ambient temperature and air. Xenon arc lamp, a light source (Newport 67005) was delivered through a Newport mono-chromator and the wavelengths of the incident light were varied from 280 to 1000 nm at 5 nm steps by using Newport utility software. Distance between focusing lenses and reference photodetector (Hamamatsu S1133-14) was maintained to focus the monochromatic light onto the reference photodetector. Output voltage from reference photodetector was measured in Agilent 4155C. Reference photodetector was then substituted by the sample under test at the same position. Output voltage from the sample was measured in Agilent 4155C. EQE of measured cells were calculated by comparing these output voltages. Figure 3.7 is the pictorial view of the Newport EQE measurement system.

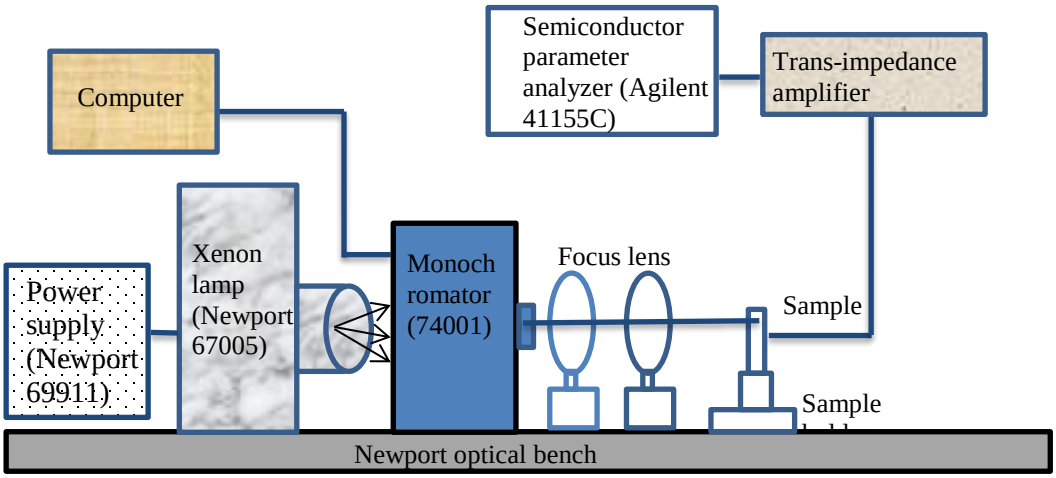

Figure 3. 6 Schematic of external quantum efficiency measurement system.

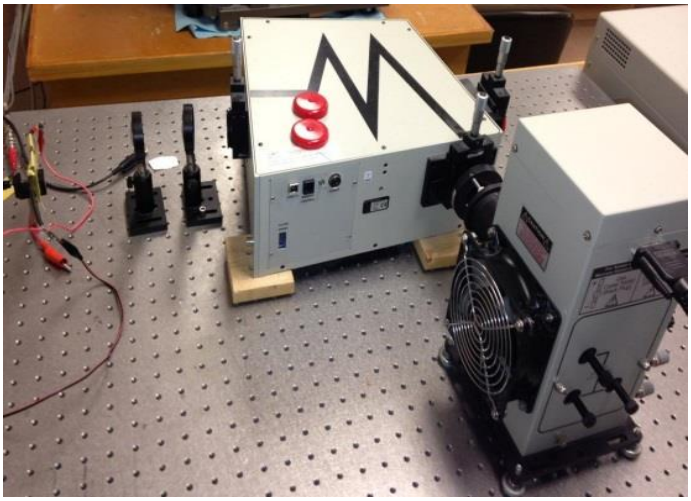

Figure 3. 7 Photograph of experimental setup for IPCE measurement

3.4. Nano morphology characterization

3.4.1 Atomic force microscopy and Kelvin probe force microscopy

For topography images, Atomic force microscopy (AFM) was operated in tapping mode using Agilent 5500 SPM (scanning probe microscope). Silicon tip (Budget Sensors, Multi75 E_g) coated with Cr/Pt was used whose had some specialty including spring constant ~1-4 N/m and tip radius of ~1A^o and resonance frequency ~75 KHz. In order to get required resolution of resonance frequency, an off-resonance of 100-200 Hz was applied to the cantilever. Without or with different interfacial layer coated Perovskite samples were observed for topographic image and surface potential respectively. Figure 3.8 shows the photograph of AFM (also KPFM) instrument (Agilent Nano-scope 5500 SPM). Gwyddion software was used to investigate the AFM images.

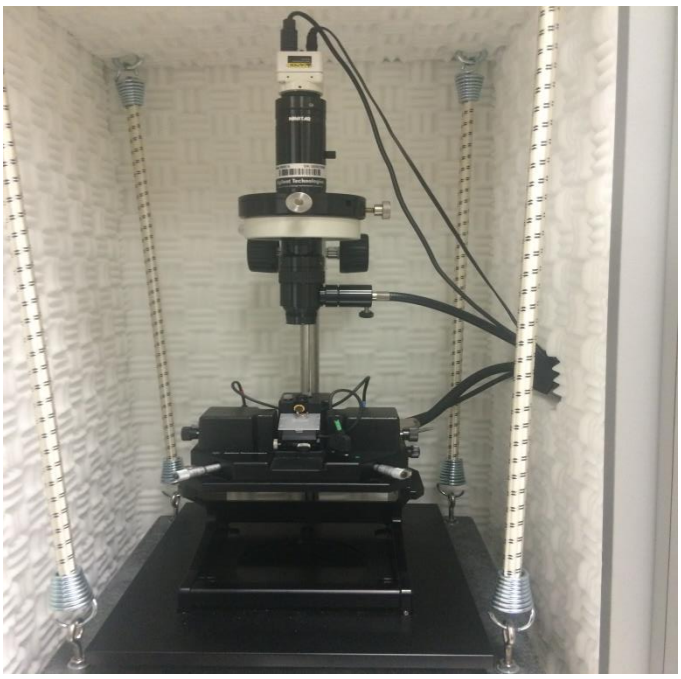

Figure 3. 8 Photograph of atomic force microscope

For surface potential measurement, first resonance (f_1) frequency of 67 kHz was fed into the first lock-in amplifier (LIA_1) used for topographic and phase imaging. The second frequency (f_2) of 5 kHz was fed into the second lock-in amplifier (LIA_2) used for KPFM measurement. An electrostatic force was created between the tip and sample by providing a 5 KHz oscillation to the tip. A certain dc offset was applied to the tip to nullify the electrostatic interaction. To achieve amplitude of 0.2 V of dc off set, the drive percentage of LIA_2 was reached around 15%. This dc bias recorded at each point provided the local CPD or surface potential. SP vs. z spectroscopy was maintained to avoid the topography interference with surface potential measurement.

3.4.2 Ultraviolet-visible spectroscopy

UV-Vis absorption of different layer coated films were taken using Agilent 8453 spectrophotometer with chem station software. Figure 3.9 shows the photograph of

ultraviolet-visible spectroscopy. Before measuring the absorption, ITO coated blank substrate was measured to remove the noise due to air and ITO glass. Then the absorption measurement was followed according to the condition of the sample.

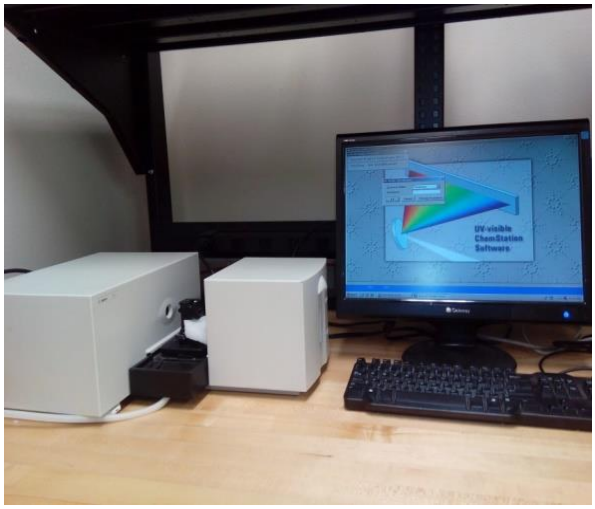

Figure 3. 9 Photograph of HP Agilent 8453 UV-Visible spectrometer

3.4.3 X-ray diffraction

Figure 3.10 shows a photograph of X-ray diffractometer (Rigaku smart lab operation system). First of all X-ray was ramped up to 40kV tube voltage and 20 mA tube current to generate X-ray of 1.54 A^{o}. Thin film measurement was then performed using a general (medium resolution PB/PSA) out of plane measurement. Optical alignment, sample alignment and general measurement were performed by inserting the parameters for scan with a step of 0.01 degree.

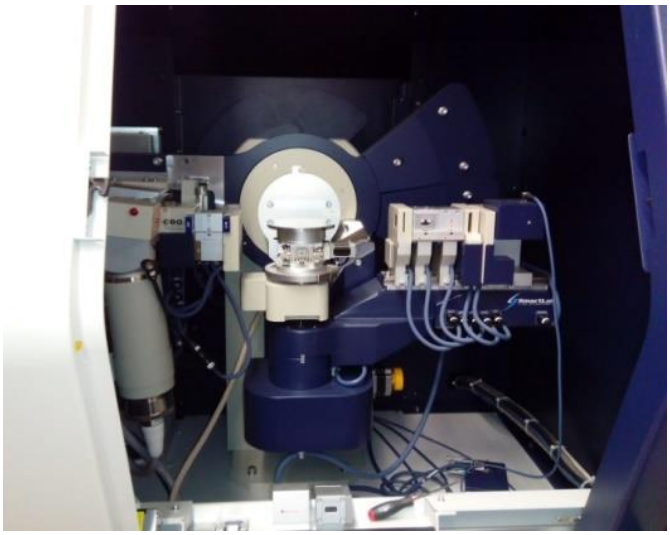

Figure 3. 10 Photograph of X-ray diffractometer (Rigaku)

3.4.4 Scanning electron microscope (SEM)

SEM images were taken in a Hitachi S-3400N SEM instrument shown in figure 3.11. The surface morphology perovskite film, $PC_{60}BM$ and with or without CBL coated perovskite films were observed using SEM with an accelerating voltage of 10 kV with working distance of ~10 mm and a magnification of 10 K. A thin layer of conducting gold (10 nm thickness) were deposited on each film and then mounted on top of a circular sample holder under a vacuum environment inside the SEM chamber.

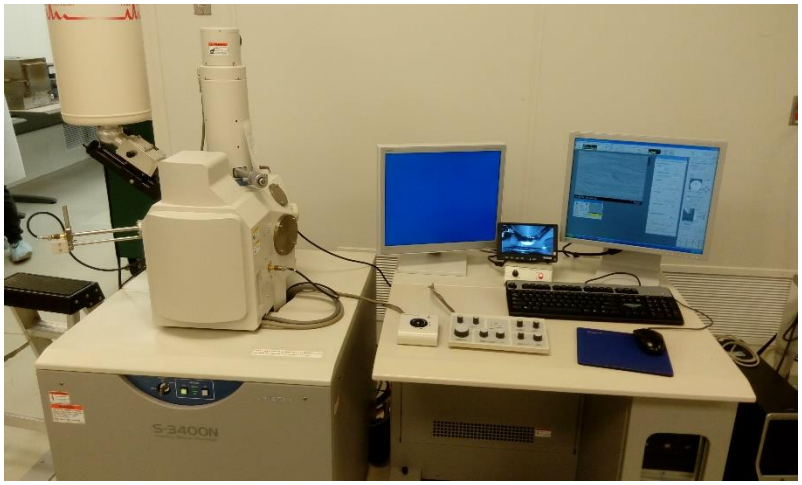

Figure 3. 11 Photograph of Hitachi S-3400N SEM

3.4.5 Transient photovoltage / photocurrent spectroscopy

The dye laser (Model 1011, repetition rate ~ 4 Hz, pulse duration < 1 ns) coupled with the nitrogen laser (OBB's Model OL-4300, crisp pulse at 337 nanometers) was used to generate pulses at specific wavelength to create a short transient decay in the cell. Figure 3.12 shows the experimental photograph of transient photo voltage and photo current measurement. A splitter was used to transmit the laser on the solar cell and photodiode simultaneously. The generated signals from the cell and photodiode were recorded in oscilloscope (Agilent MSO-X-4154A, 1.5 GHz, 5 Gsa/sec). The transient photocurrent decay was measured at short circuit condition using 50 Ω resistance of the oscilloscope. On the other hand, the Transient photo-voltage decay was measured at open circuit condition under light illumination and steady state condition using 1 MΩ resistance of the oscilloscope. For finding the charge transport time and charge carrier life time of the perovskite solar device, the achieved decays were fitted with mono exponentially decaying function.

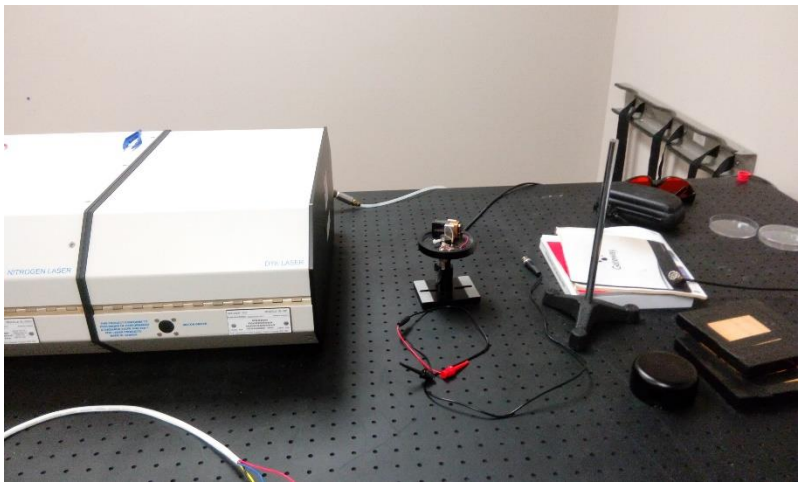

Figure 3. 12 TPC and TPV experimental set up

Chapter 4. Results and Analysis

4.1 UV-visible spectrum and external quantum efficiency (EQE)

Perovskite solar cell's active light absorbing layer is sandwiched between the electron transport layer (ETL) and hole transport layer (HTL). It was noticed that the enhancement of efficiency by using CBL in between the ETL and the metal electrode, Ag. So it was fabricated with the device structure like glass/ITO/PEDOT: PSS (HTL)/perovskite/PCBM (ETL)/CBL/Ag. Figure 4.1 (a) shows the UV-visible absorption spectra of CBL deposited on the top of glass/ITO/PEDOT: PSS /perovskite/PCBM. It was observed that CBL coated using PVP, provided broader absorption near 400-800 nm compared to CBL coated using Rhodamine and without CBL.

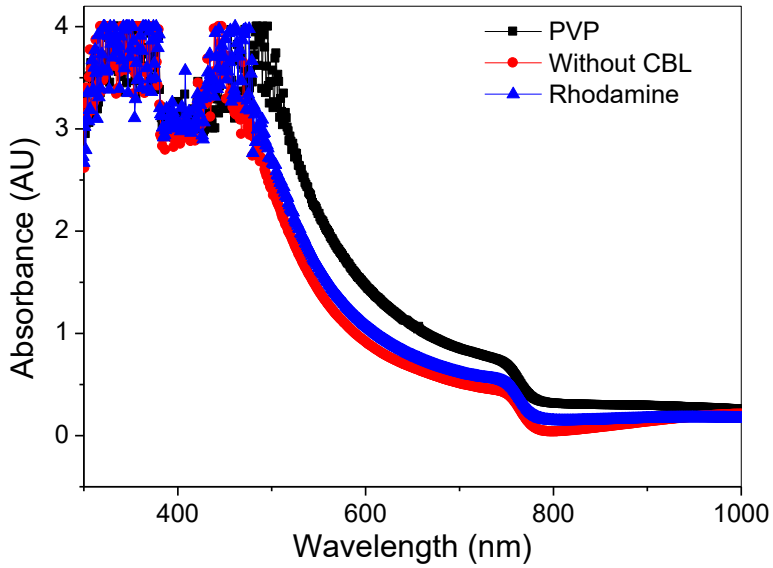

Figure 4. 1 UV-visible absorbance spectra of PCBM films with CBL (PVP and Rhodamine) and without CBL (PCBM only).

4.2 XRD measurement of perovskite solar cell

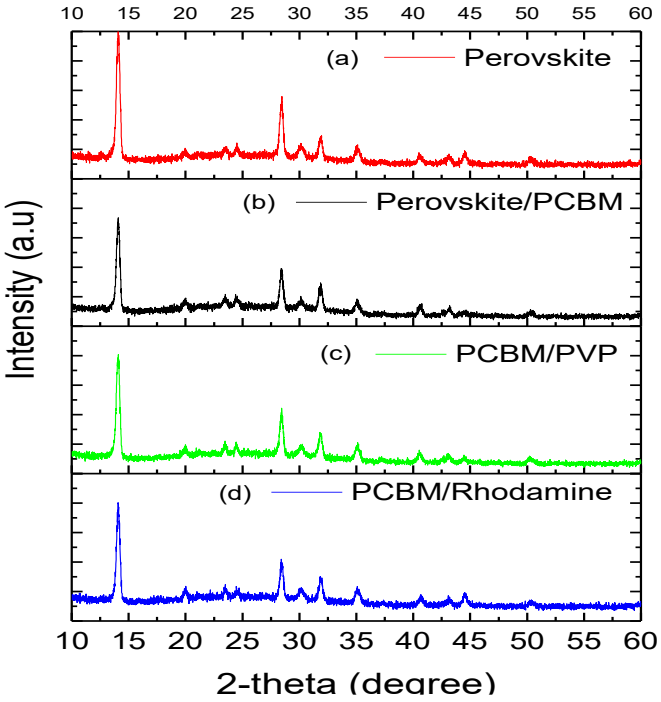

Figure 4. 2 XRD spectra (a) Perovskite only (b) Perovskite /PCBM layer (c) Perovskite /PCBM/PVP layer (d) Perovskite /PCBM/Rhodamine layer

Figure 4.2 shows XRD spectra of different film placed on the upper surface of the perovskite layer. The peak intensity at 14^{o} and 28^{o} were occurring for 110 and 220 planes which ensured the complete crystallization of perovskite phase. Figure 4.2 (b), (c), (d) showed no difference of peaks if PCBM and other CBL were deposited on the top of perovskite film. All the cases, it concluded the formation of orthorhombic crystal structure of perovskite with high crystallinity.

4.3 J-V characteristics of perovskite solar cell

Figure 4.3 shows the current density-voltage (J-V) characteristics of PSCs with reverse and forward scan. The J-V characteristics were performed at same condition with same scan rate for all the cells. PSCs were fabricated with three different spin coating speed

(1000 rpm, 3000 rpm and 5000 rpm) using PVP as CBL in p-i-n planar structure. The thickness of CBL played a vital role for improving device performance. The slower spin coating speed makes comparatively thicker film than higher spin coating speed. The thicker film attributed to less charge transport and provided less short circuit current density.

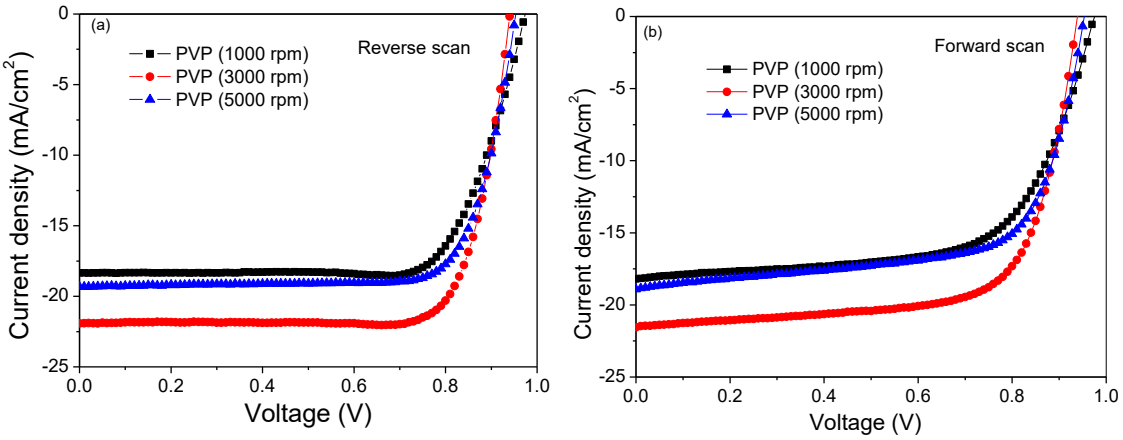

Figure 4. 3 Current density-voltage characteristics of PSCs with PVP as CBL (a) reverse scan (b) forward scan.

When the spin coating speed of PVP buffer layer was 5000 rpm, J_{sc} and V_{oc} started to decrease due to non-uniform layer distribution and created less dipole moment in the interface. Table 4.1 shows the performance determining parameters of PSCs. PVP as CBL based PSCs showed higher PCE of 16.35% (reverse scan) while the spin speed of PVP layer was 3000 rpm. As PVP is non-conjugated polymer, the optimum thinness were achieved by changing the rpm speed of spin coater. There were different PCE's for reverse and forward scan due to the presence of hysteresis effect of perovskite materials.

Table 4. 1 Performance determining parameters of Perovskite solar cell

Conditions		J_{sc} (mA/cm^2)	V_{oc} (V)	FF	PCE (%)
With PVP (1000 rpm)	Reverse	-18.54	0.98	0.74	13.51
	Forward	-18.23	0.98	0.64	11.42

With PVP (3000 rpm)	Reverse	-22.03	0.95	0.78	16.35
	Forward	-21.57	0.94	0.70	14.10
With PVP (5000 rpm)	Reverse	-19.32	0.96	0.80	14.96
	Forward	18.91	0.95	0.67	12.10

Figure 4.4 also shows the J-V characteristics of PSCs in both reverse and forward scan with different concentrations (0.5-2.0 mg/ml) of PVP material dissolved in isopropanol (IPA). Starting from 0.5 mg/ml IPA, the J_{sc} and FF increased with the increase of PVP concentration. After 1 mg/ml then it started to decrease and the concentration was optimized. The higher concentrations of PVP hinders charge transport and creates recombination which reduces the short circuit current density and fill factor. Table 4.2 also shows different parameters of PSCs with different concentrations of PVP as CBL material.

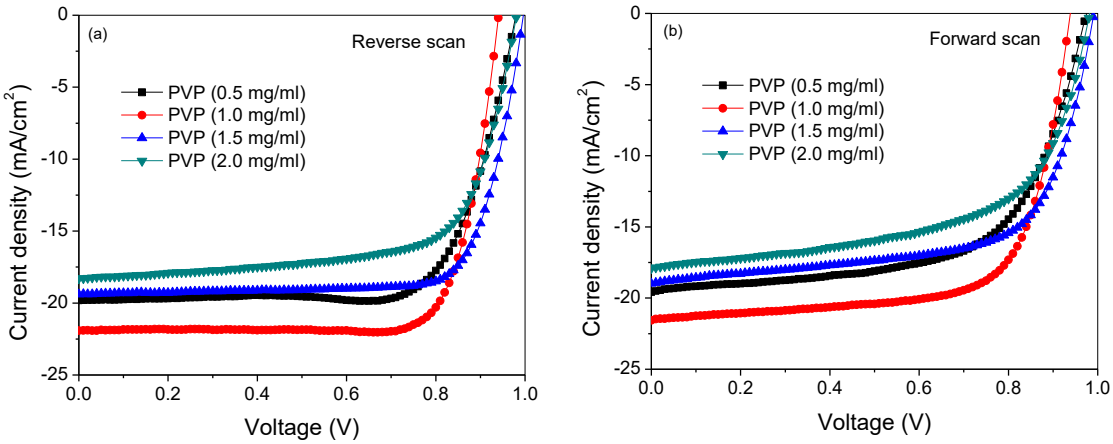

Figure 4. 4 J-V characteristics of PSCs (a) reverse scan (b) forward scan with different concentration of PVP

Table 4. 2 Performance determining parameter of solar cell

Concentration	Scan	J_{sc} (mA/cm^2)	V_{oc} (V)	FF	PCE (%)
PVP (0.5 mg/ml)	Reverse	-19.87	0.98	0.74	14.35
	Forward	-19.58	0.98	0.62	11.89

PVP (1.0 mg/ml)	Reverse	-22.03	0.95	0.78	16.35
	Forward	-21.57	0.94	0.70	14.10
PVP (1.5 mg/ml)	Reverse	-19.38	1.00	0.76	14.92
	Forward	-18.98	0.99	0.65	12.35
PVP (2.0 mg/ml)	Reverse	-18.28	0.99	0.68	12.37
	Forward	17.90	0.98	0.59	10.44

Figure 4.5 shows the J-V characteristics of best devices with optimized PVP concentration and layer thickness compared to another CBL (Rhodamine) and without CBL. The best PSC achieved PCE of 16.35% efficiency which is the highest reported efficiency using non-conjugated polymer materials used in perovskite solar cell so far. The comparative device parameters have been listed in Table 4.3.

Figure 4.5 (b) shows the plot of EQE of a complete PSC fabricated with or without any CBL. It was also confirmed from the figure that PVP as CBL based perovskite solar cell had average of 80% EQE compared to another CBL (Rhodamine) and without CBL. In the range of 650nm-750nm, the EQE difference was highly noticeable and also confirmed by the short circuit current density (J_{sc}) obtained from the J-V characteristics. The J_{sc} obtained from EQE integration over AM 1.5 solar simulator spectrum was almost identical to the experimentally obtained J-V characteristics.

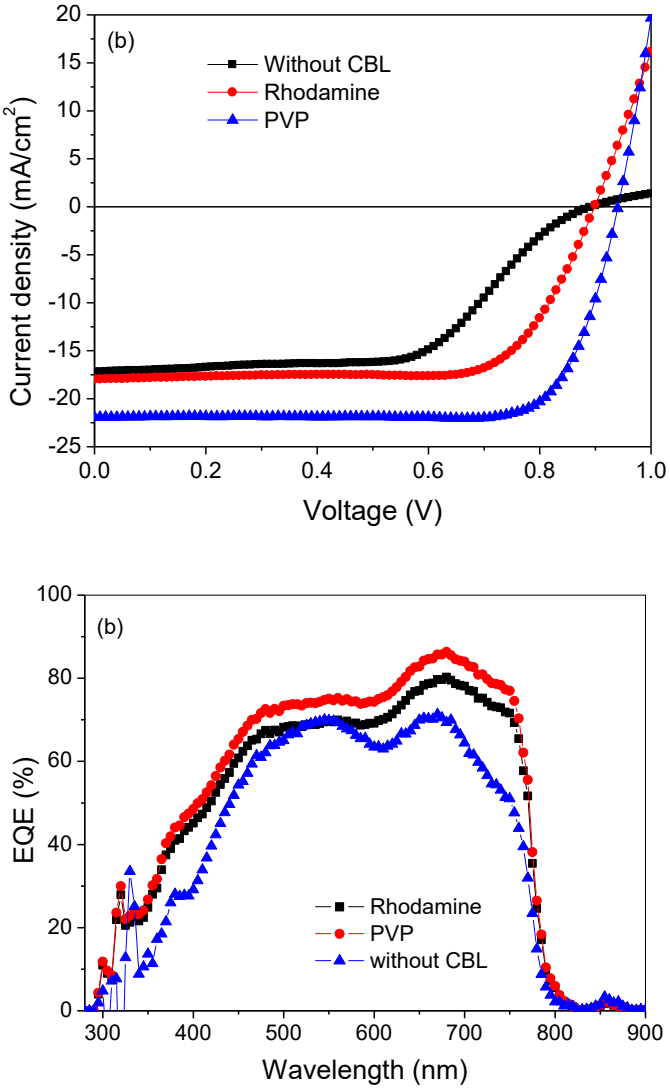

Figure 4. 5 (a) J-V characteristics of PSCs with optimized (best) conditions with (PVP and Rhodamine) and without CBL. (b) External quantum efficiency (EQE) of different CBLs (PVP and Rhodamine) and without CBL (PCBM only)

Table 4. 3 perovskite solar cell parameters

Condition	J_{sc} (mA/cm^2)	V_{oc} (V)	FF	PCE (%)
PVP	-22.03	0.95	0.78	**16.35**
Rhodamine	-17.97	0.90	0.77	12.45
Without CBL	-17.21	0.90	0.58	8.97

Figure 4.6 shows the reproducibility of PSCs parameters. Simultaneous enhancement of J_{sc}, V_{oc}, FF and PCEs observed when at least 10 devices were made with or without CBL.

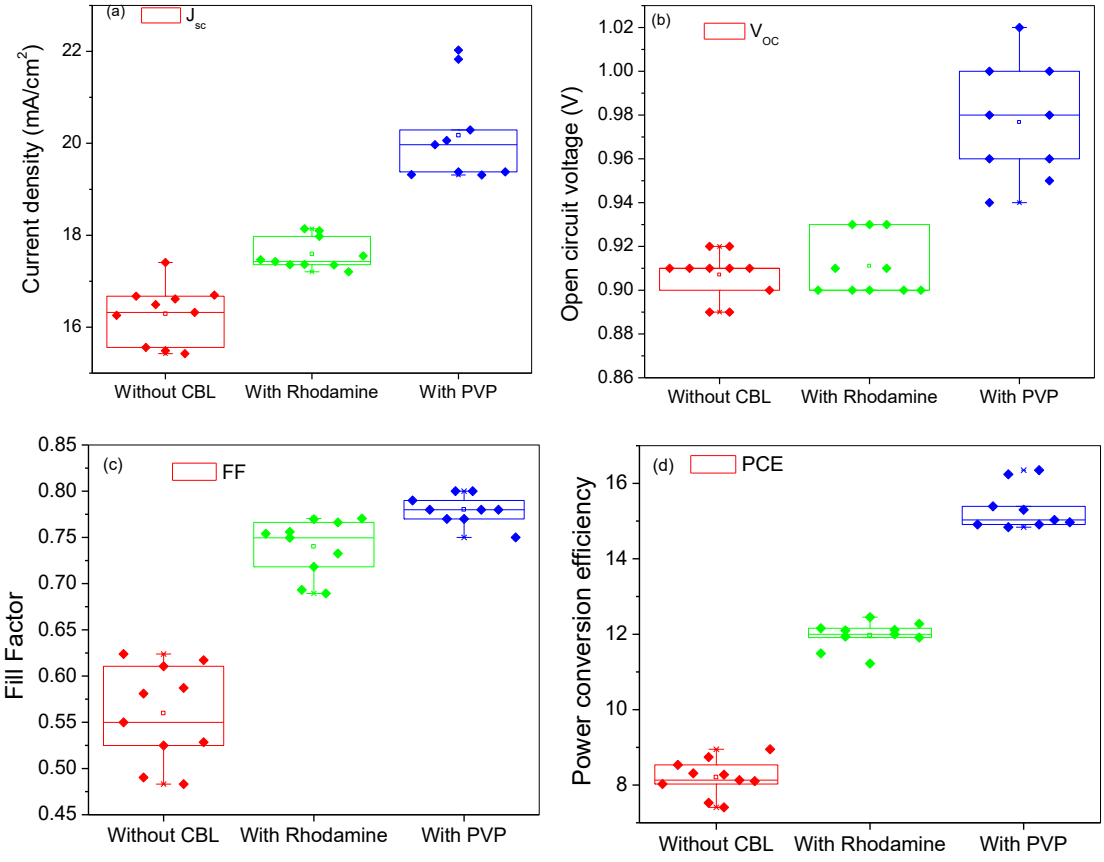

Figure 4. 6 Reproducibility of PSCs parameters (a) short circuit current density, J_{sc} (b) open circuit voltage, V_{oc} (c) fill factor, FF and (d) efficiency, PCE

4.4 Nano morphology characterization

Figure 4.7 shows the atomic force microscopy (AFM) and scanning electron microscopy (SEM) images of perovskite film. AFM image showed the crystal formation

in the 5µm ×5µm area and SEM image showed the surface morphology with complete coverage.

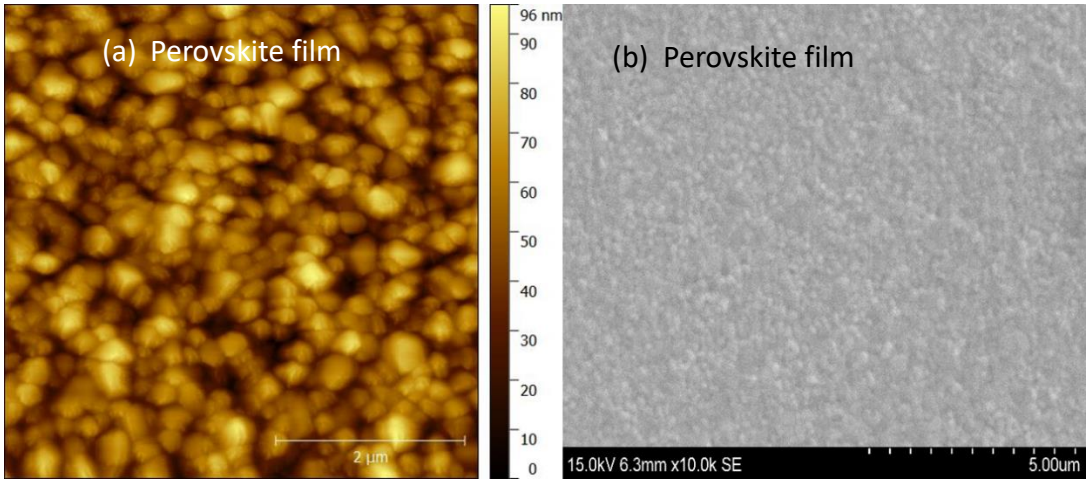

Figure 4. 7 (a) Atomic force microscopy (AFM) topography and (b) scanning electron microscopy (SEM) image of perovskite film

Figure 4.8 shows the kelvin probe force microscope (KPFM) images of PCBM, PCBM/PVP and PCBM/Rhodamine films. The topography of PCBM film (without CBL) showed RMS value of 75.93 nm, while the roughness decreased with incorporation of interfacial materials. The lowest RMS achieved was about 23.36 nm for PVP as CBL. Lower roughness and smooth surface enhances the charge transport, hence increase J_{sc}. The surface potential images explained the enhancement of V_{oc}. The film without CBL provided a more negative value whereas PVP as CBL values increased positively which might be the reason for the enhancement of V_{oc}. There might be another reason why V_{oc} increase is due to the formation of dipole in between the PCBM and Ag.

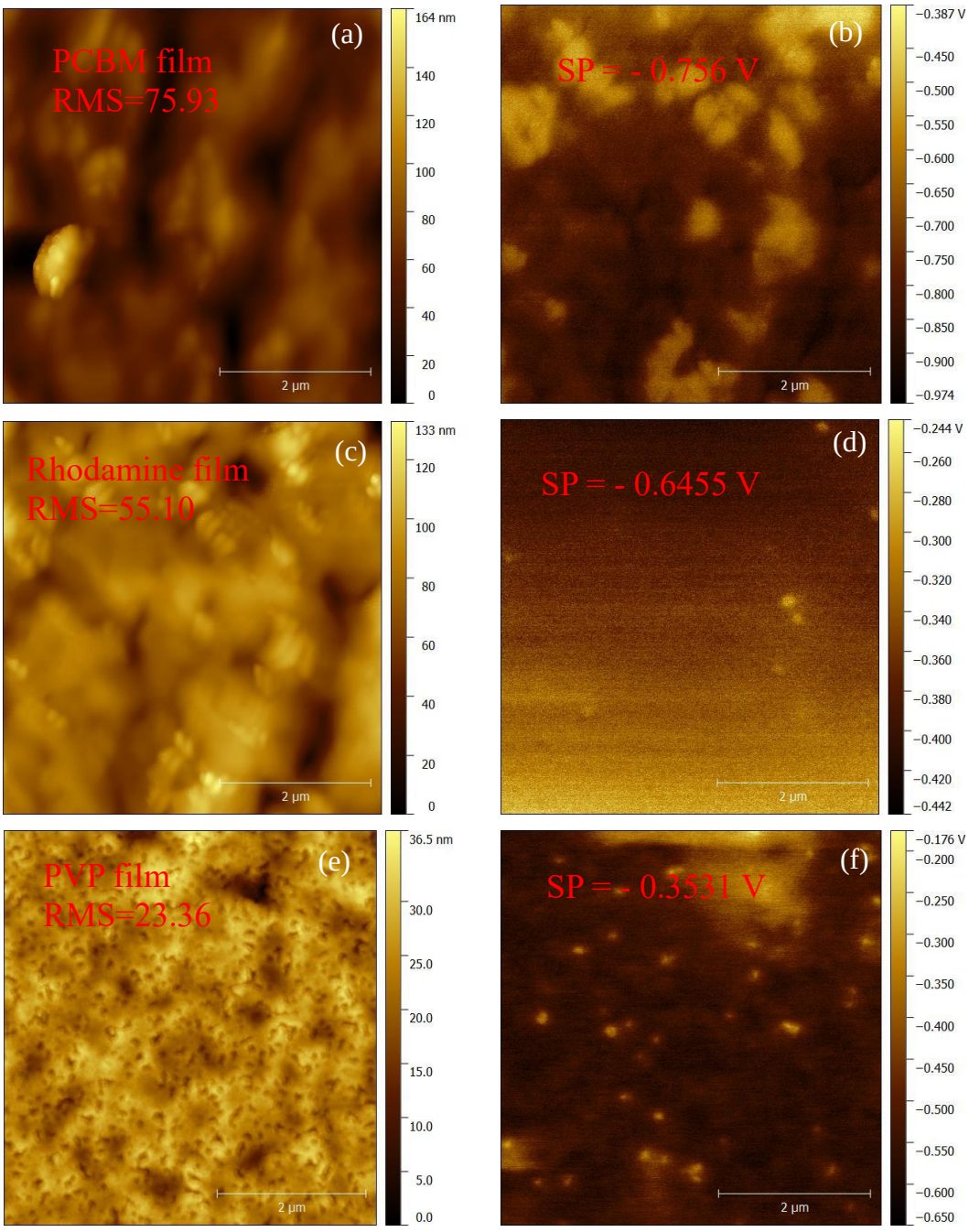

Figure 4. 8 Topographic images of (a) PCBM (c) Rhodamine (e) PVP films and surface potential images of (b) PCBM (d) Rhodamine (f) PVP films

Figure 4.9 shows the surface potential (SP) distribution of PCBM films coated on the top of perovskite with and without CBL. SP increased with incorporation of PVP as CBL due to the reduction of surface defects of PCBM film. The increase in surface potential led to higher V_{oc} for PVP layered PSC compared to without CBL.

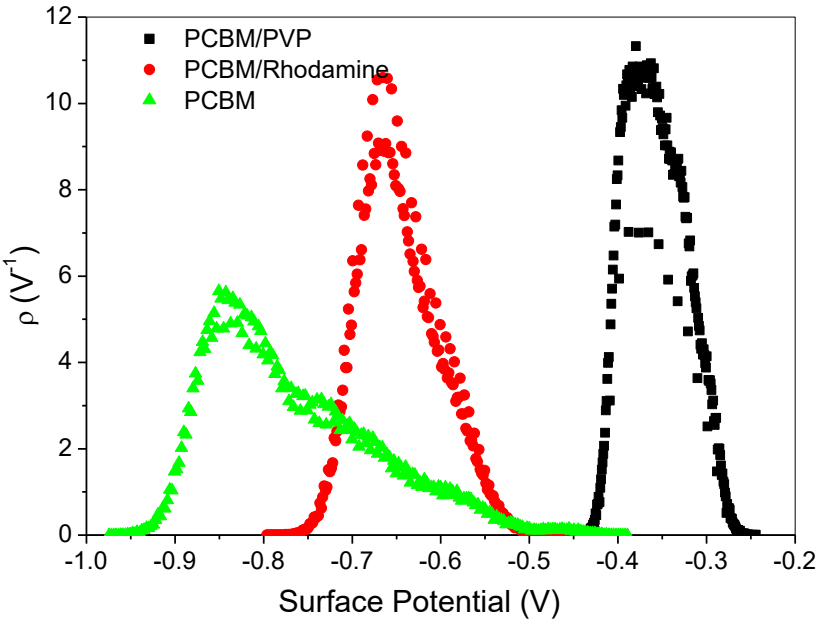

Figure 4. 9 Surface potential distribution of PCBM with and without CBL

Figure 4.10 (a) shows the SEM image of PCBM film where there was noticed some pinholes present in the surface morphology. On the other figure 4.10 (b) showed surface morphology with complete coverage and no pinholes when PVP was used as CBL. The pinhole free and smooth film improves the charge transport and overall device performances.

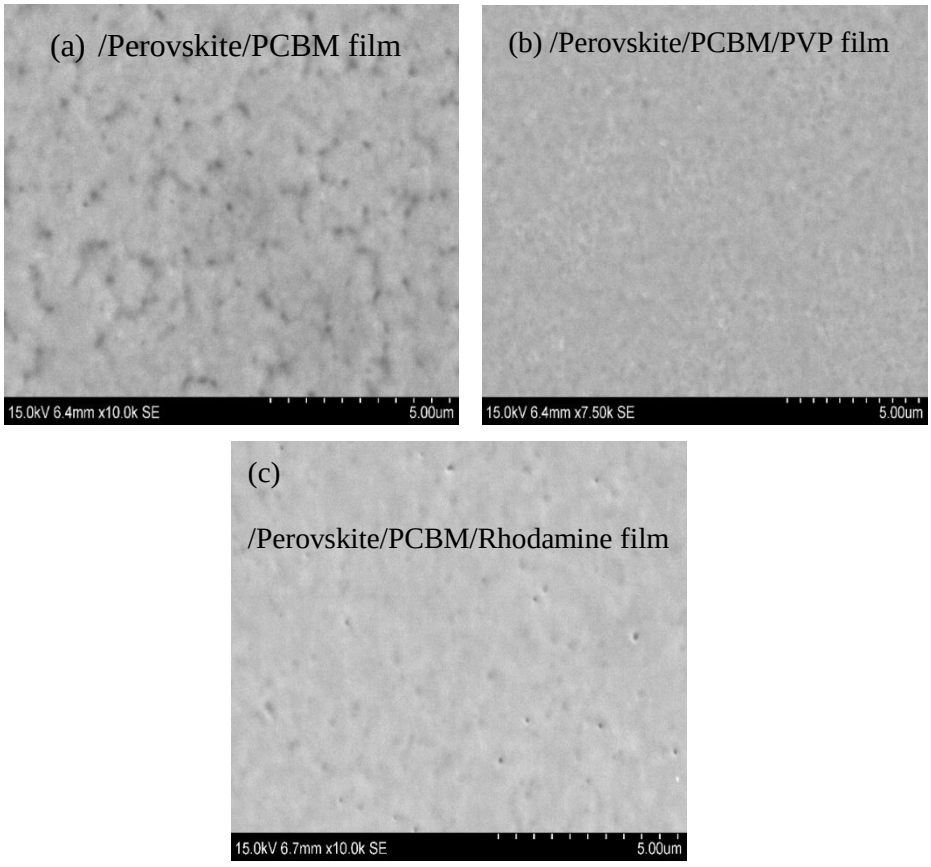

Figure 4. 10 SEM images of (a) /Perovskite/PCBM film (b) /Perovskite/PCBM/PVP film (c) /Perovskite/PCBM/Rhodamine film

4.5 Transient photocurrent and photo voltage measurement

Figure 4.11 shows the transient photocurrent measurement. The device without CBL provided charge transport time of 0.985 μS while it reduced to 0.636 μS when PVP was used as CBL. The device made using rhodamine also provided charge transport time of 0.835 μS compared to without CBL which confirmed the enhancement of FF. The faster the charge transport time, the better is the device performances.

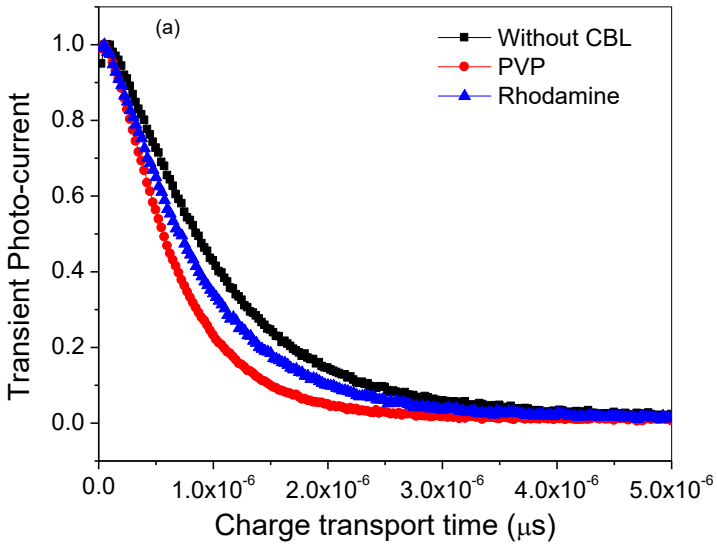

Figure 4. 11 Transient photo current measurement of different device made from without and with CBL (PVP and Rhodamine)

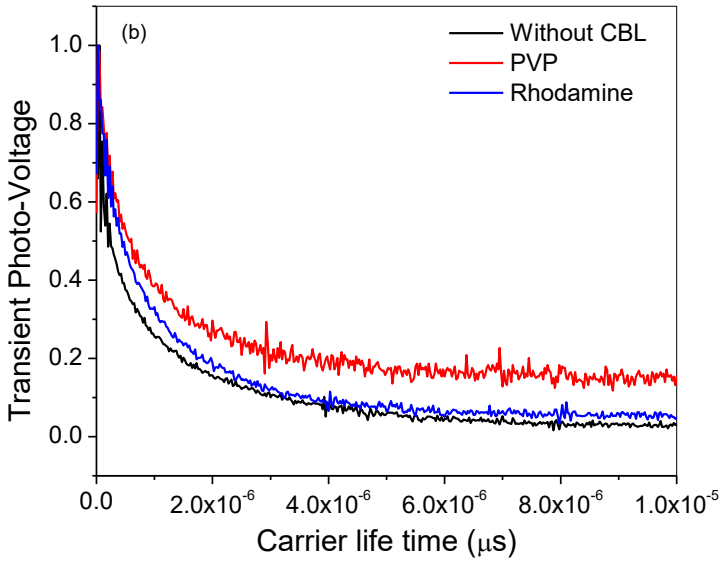

Figure 4. 12 Transient photo current measurement of different device made from without and with CBL (PVP and Rhodamine)

Figure 4.12 shows the transient photo-voltage measurement. The device without CBL provided charge carrier lifetime of 0.939 µS while it increased to 1.192 µS when PVP

was used as CBL. A high carrier lifetime suppresses the charge carrier recombination and increases the device performances. The parameters from transient measurement are given in the Table 4.4.

Table 4. 4 Charge transport time and carrier life time

Condition	**Charge transport time**	**Carrier lifetime**
Without CBL	0.985 (μS)	0.939 (μS)
PVP	0.636 (μS)	1.192 (μS)
Rhodamine	0.835 (μS)	1.078 (μS)

Chapter 5. Summary and Conclusions

5.1 Summary

Alternative sources such as thermal, wind, hydro, etc. are getting priority of energy to fulfill the energy demands. But they are not available all the time and requires huge installation cost. To keep the environment free from the pollution, solar energy is highly recommended with lower cost. Starting from the first generation of Si solar cell, it has been reached to 24% efficiency. Also, thin film PV devices made from inorganic III-V semiconductor is also overcoming the demand of energy with producing PCE about 44.6%. However, the producers are always in necessity of low cost, solution process and highly efficient solar cells. Unlike inorganic Si solar cells, OPVs, DSSCs and next generation PSCs have been widely examined due to lower cost and higher efficiency.

The principle of SCs comes from photovoltaic effect. When a photon incidents on a semiconductor material, an electron from the ground state is excited to the higher energy states. In order to take place this phenomenon, the photon energy must be higher than the forbidden energy gap of that specific semiconductor material. It is the so called absorption of photons. In photovoltaic devices, due to absorption process, a built in electric field is produced. However, excited electrons are extracted to the external circuit before they relax back to the ground state. Basically a p-type semiconductor and n-type semiconductor is being formed a junction where p-type is made from doping by Boron (B) or Aluminum (Al) and n-type is made from doping by Phosphorous (P) or Arsenic (As). The efficiency of a solar cell is considered the most performance determining parameters which depends on short circuit current density, J_{sc} and open circuit voltage, V_{oc} and fill factor, FF.

The molecular structure of perovskite is ABX_3, where A and B are the cations and X symbolizes the halide group as an anion. Most commonly used perovskite absorber layer is the combination of MAI and PbI_2 where methylammonium iodide (CH_3NH_3I or MAI) is the organic part which facilitates self-assembly and lead iodide (PbI_2) is the inorganic salt which provides an extended network by covalent or ionic interaction that allows for precise crystalline structure formation. The electronic and optical properties are determined by the ratio of halide ions.

Although the device structure was retrieved from dye DSSCs, Miyasaka first fabricated PSC in 2009 with PCE of 3.8%. However, it was not stable for longer time due to the liquid electrolyte which damage perovskite film very quick. After that, a long term stable perovskite solar cell was reported with PCE of 9.7% by Park *et al.* in 2012. Saliba *et al.* reported the world's highest efficiency of PSCs in 2016 with PCE of 22.1%. Numerous device architectures have been designed and investigated for constructing PSCs consisting of different ETLs and HTLs with respective metal electrodes (Ca, Al, Ag etc.). For fabricating PSCs, different fabrication and deposition technique have been investigated including two step dip coating, two step spin coating, single step spin coating, stamping, thermal evaporation, vapor assisted solution processing, vacuum pump method and so on. It is highly important to consider energy band diagram (LUMO and HOMO level) to facilitate faster charge transport and longer carrier life time. The buffer layer between ETL and metal electrode plays an important role in this regard.

Perovskite films were fabricated as explained before in experimental procedure sections. For the first time, PVP was used as a CBL in case of PSCs. The prepared films with and without CBL were then characterized using UV-vis spectroscope, XRD, AFM,

KPFM and SEM. J-V characteristics were measured using semiconductor parameter analyzer (Agilent 4155C) combined with a xenon lamp (Newport 67005) as solar simulator (AM 1.5). EQE was measured using a Newport kit with a 7412 Oriel Cornerstone 260 ¼m mono-chromator in ambient temperature. The CBLs (PVP or rhodamine) were deposited on the top of PCBM using spin coating technique. The final devices achieved PCE more than 14%. The CBL shows a significant part in device performance by enhancing the FF and short circuit current density. The optimum film thickness and CBL material's concentration are required for high performance perovskite solar cell.

5.2 Conclusions

Finally, the use of non-conjugated polymer PVP as CBL achieved an efficiency of 16.35%, which was significantly higher than the 12.45% using Rhodamine and 8.97% without CBL. There were simultaneous enhancements in Jsc, FF, Voc and overall PCE due to use of PVP as CBL. The highest device achieved a PCE of 16.35%, which has been the highest reported efficiency in perovskite solar cell using non-conjugated polymer materials. The enhancement in device performance might be caused by the smoother films, lower surface potential and formation of dipole between the ETL and Ag electrode. Therefore, PVP can be used as effective CBL material in the planar p-i-n device structure to achieve low cost, solution processible and high efficiency perovskite solar cells.

5.3 Future work

Future work should consider a detailed understanding of the effect of nanoscale grain boundaries of CBL in perovskite solar cell with increasing the concentration more than 2mg/ml IPA as well as check the stability to obtain efficiency greater than 20%.

References:

[1] L. Pérez-Lombard, J. Ortiz, and C. Pout, "A review on buildings energy consumption information," *Energy and buildings,* vol. 40, no. 3, pp. 394-398, 2008.

[2] J. Darmstadter, P. D. Teitelbaum, and J. G. Polach, "Energy in the world economy," 1970.

[3] Y. Ogomi *et al.*, "CH3NH3Sn x Pb (1–x) I3 Perovskite Solar Cells Covering up to 1060 nm," *The Journal of Physical Chemistry Letters,* vol. 5, no. 6, pp. 1004-1011, 2014.

[4] C. R. E. Becquerel, "Recherches sur les effets de la radiation chimique de la lumiere solaire au moyen des courants electriques", Comptes Rendus de L´Academie des Sciences" 9, 561(1839).

[5] G. Liobikienė and M. Butkus, "The European Union possibilities to achieve targets of Europe 2020 and Paris agreement climate policy," *Renewable Energy,* vol. 106, pp. 298-309, 2017.

[6] Albert Einstein (in 1905) "discovery of photoelectric effect" retrieved from http://en.wikipedia.org/wiki/Photoelectric_effect.

[7] N. R. E. Laboratory. (2017). *Solar Cell Efficency Performance*. Available: http://www.nrel.gov/

[8] Fritts C, Proceedings of the American Association for the Advancement of Science 33, 97 (1883).

[9] C. F. D. Chapin, and G. Pearson, J. Appl. Phys., 25, 676 (1954).

[10] J. Zhao, A. Wang, M. A. Green, and F. Ferrazza, "19.8% efficient "honeycomb" textured multicrystalline and 24.4% monocrystalline silicon solar cells," *Applied Physics Letters,* vol. 73, no. 14, pp. 1991-1993, 1998.

[11] S. Seo, J. Lee, E.-J. Choi, E.-J. Kim, J.-Y. Song, and J. Kim, "Polydiacetylene Liposome Microarray Toward Influenza A Virus Detection: Effect of Target Size on Turn-On Signaling," *Macromolecular Rapid Communications,* vol. 34, no. 9, pp. 743-748, 2013.

[12] Y. S. Tyan and E. A. Perez-Albuerne, "Integrated array of photovoltaic cells having minimized shorting losses," ed: Google Patents, 1982.

[13] C. W. Tang, "Two-layer organic photovoltaic cell," *Applied Physics Letters,* vol. 48, no. 2, pp. 183-185, 1986.

[14] H. Spanggaard and F. C. Krebs, "A brief history of the development of organic and polymeric photovoltaics," *Solar Energy Materials and Solar Cells,* vol. 83, no. 2, pp. 125-146, 2004.

[15] H. Hoppe and N. S. Sariciftci, "Polymer solar cells," in *Photoresponsive Polymers II*: Springer, 2008, pp. 1-86.

[16] G. Yu, J. Gao, J. C. Hummelen, F. Wudl, and A. J. Heeger, "Polymer Photovoltaic Cells: Enhanced Efficiencies via a Network of Internal Donor-Acceptor Heterojunctions," *Science,* vol. 270, no. 5243, pp. 1789-1791, 1995.

[17] S. E. Shaheen, C. J. Brabec, N. S. Sariciftci, F. Padinger, T. Fromherz, and J. C. Hummelen, "2.5% efficient organic plastic solar cells," *Applied Physics Letters,* vol. 78, no. 6, pp. 841-843, 2001.

[18] L. Dou *et al.*, "Tandem polymer solar cells featuring a spectrally matched low-bandgap polymer," *Nature Photonics,* vol. 6, no. 3, pp. 180-185, 2012.

[19] J. Hou *et al.*, "Bandgap and molecular energy level control of conjugated polymer photovoltaic materials based on benzo [1, 2-b: 4, 5-b′] dithiophene," *Macromolecules,* vol. 41, no. 16, pp. 6012-6018, 2008.

[20] J. Moser, "Notiz über Verstärkung photoelektrischer Ströme durch optische Sensibilisirung," *Monatshefte für Chemie und verwandte Teile anderer Wissenschaften,* journal article vol. 8, no. 1, pp. 373-373, 1887.

[21] B. O'regan and M. Grfitzeli, "A low-cost, high-efficiency solar cell based on dye-sensitized," *nature,* vol. 353, p. 24, 1991.
[22] A. Yella *et al.*, "Porphyrin-sensitized solar cells with cobalt (II/III)–based redox electrolyte exceed 12 percent efficiency," *science,* vol. 334, no. 6056, pp. 629-634, 2011.
[23] M. A. Green, A. Ho-Baillie, and H. J. Snaith, "The emergence of perovskite solar cells," *Nature Photonics,* vol. 8, no. 7, pp. 506-514, 2014.
[24] M. Liu, M. B. Johnston, and H. J. Snaith, "Efficient planar heterojunction perovskite solar cells by vapour deposition," *Nature,* vol. 501, no. 7467, pp. 395-398, 2013.
[25] M. M. Lee, J. Teuscher, T. Miyasaka, T. N. Murakami, and H. J. Snaith, "Efficient hybrid solar cells based on meso-superstructured organometal halide perovskites," *Science,* vol. 338, no. 6107, pp. 643-647, 2012.
[26] A. Mei *et al.*, "A hole-conductor–free, fully printable mesoscopic perovskite solar cell with high stability," *Science,* vol. 345, no. 6194, pp. 295-298, 2014.
[27] M. J. Carnie *et al.*, "A one-step low temperature processing route for organolead halide perovskite solar cells," *Chemical Communications,* vol. 49, no. 72, pp. 7893-7895, 2013.
[28] H.-S. Kim *et al.*, "Lead iodide perovskite sensitized all-solid-state submicron thin film mesoscopic solar cell with efficiency exceeding 9%," *Scientific reports,* vol. 2, 2012.
[29] S. Luo and W. A. Daoud, "Recent progress in organic–inorganic halide perovskite solar cells: mechanisms and material design," *Journal of Materials Chemistry A,* 2015.
[30] H.-S. Kim *et al.*, "High efficiency solid-state sensitized solar cell-based on submicrometer rutile TiO_2 nanorod and CH3NH3PbI3 perovskite sensitizer," *Nano letters,* vol. 13, no. 6, pp. 2412-2417, 2013.
[31] J. M. Ball, M. M. Lee, A. Hey, and H. J. Snaith, "Low-temperature processed meso-superstructured to thin-film perovskite solar cells," *Energy & Environmental Science,* vol. 6, no. 6, pp. 1739-1743, 2013.
[32] J. You *et al.*, "Low-temperature solution-processed perovskite solar cells with high efficiency and flexibility," 2014.
[33] A. Gurung *et al.*, "Highly Efficient Perovskite Solar Cell Photocharging of Lithium Ion Battery Using DC–DC Booster," *Advanced Energy Materials,* vol. 7, no. 11, pp. 1602105-n/a, 2017, Art. no. 1602105.
[34] S. Mabrouk *et al.*, "Increased Efficiency for Perovskite Photovoltaics via Doping the PbI2 Layer," *The Journal of Physical Chemistry C,* vol. 120, no. 43, pp. 24577-24582, 2016.
[35] G. Li, C.-W. Chu, V. Shrotriya, J. Huang, and Y. Yang, "Efficient inverted polymer solar cells," *Applied Physics Letters,* vol. 88, no. 25, p. 253503, 2006.
[36] H. Azimi *et al.*, "A Universal Interface Layer Based on an Amine-Functionalized Fullerene Derivative with Dual Functionality for Efficient Solution Processed Organic and Perovskite Solar Cells," *Advanced Energy Materials,* vol. 5, no. 8, 2015.
[37] F. Zhang, M. Ceder, and O. Inganäs, "Enhancing the photovoltage of polymer solar cells by using a modified cathode," *Advanced Materials,* vol. 19, no. 14, pp. 1835-1838, 2007.
[38] Z. He *et al.*, "Simultaneous enhancement of open-circuit voltage, short-circuit current density, and fill factor in polymer solar cells," *Advanced Materials,* vol. 23, no. 40, pp. 4636-4643, 2011.
[39] F.-C. Chen and S.-C. Chien, "Nanoscale functional interlayers formed through spontaneous vertical phase separation in polymer photovoltaic devices," *Journal of Materials Chemistry,* vol. 19, no. 37, pp. 6865-6869, 2009.
[40] S. Yamakawa, K. Tajima, and K. Hashimoto, "Buffer layer formation in organic photovoltaic cells by self-organization of poly (dimethylsiloxane) s," *Organic Electronics,* vol. 10, no. 3, pp. 511-514, 2009.
[41] K.-G. Lim, M.-R. Choi, H.-B. Kim, J. H. Park, and T.-W. Lee, "High-efficiency polymer photovoltaic cells using a solution-processable insulating interfacial nanolayer: the role of

the insulating nanolayer," *Journal of Materials Chemistry,* vol. 22, no. 48, pp. 25148-25153, 2012.

[42] H. Zhang *et al.*, "Improved high-efficiency perovskite planar heterojunction solar cells via incorporation of a polyelectrolyte interlayer," *Chemistry of Materials,* vol. 26, no. 18, pp. 5190-5193, 2014.

[43] Q. Xue *et al.*, "Highly efficient fullerene/perovskite planar heterojunction solar cells via cathode modification with an amino-functionalized polymer interlayer," *Journal of Materials Chemistry A,* vol. 2, no. 46, pp. 19598-19603, 2014.

[44] J. Min *et al.*, "Interface engineering of perovskite hybrid solar cells with solution-processed perylene–diimide heterojunctions toward high performance," *Chemistry of Materials,* vol. 27, no. 1, pp. 227-234, 2014.

[45] T. M. Thi, L. Van Tinh, B. H. Van, P. Van Ben, and V. Q. Trung, "The effect of polyvinylpyrrolidone on the optical properties of the Ni-doped ZnS nanocrystalline thin films synthesized by chemical method," *Journal of Nanomaterials,* vol. 2012, p. 3, 2012.

[46] Y. Guo, K. Shoyama, W. Sato, and E. Nakamura, "Polymer stabilization of lead (II) perovskite cubic nanocrystals for semitransparent solar cells," *Advanced Energy Materials,* 2016.

[47] Q. Wang, Y. Shao, Q. Dong, Z. Xiao, Y. Yuan, and J. Huang, "Large fill-factor bilayer iodine perovskite solar cells fabricated by a low-temperature solution-process," *Energy & Environmental Science,* vol. 7, no. 7, pp. 2359-2365, 2014.

[48] J. Y. Jeng *et al.*, "CH3NH3PbI3 Perovskite/Fullerene Planar-Heterojunction Hybrid Solar Cells," *Advanced Materials,* vol. 25, no. 27, pp. 3727-3732, 2013.

[49] Q. Qiao, "EE 735 - Fundamental of photovoltaics " *South Dakota State University* 2016.

[50] K. Aleksandrov and V. Beznosikov, "Hierarchies of perovskite-like crystals (Review)," *Physics of the Solid State,* vol. 39, no. 5, pp. 695-715, 1997.

[51] C. Kagan, D. Mitzi, and C. Dimitrakopoulos, "Organic-inorganic hybrid materials as semiconducting channels in thin-film field-effect transistors," *Science,* vol. 286, no. 5441, pp. 945-947, 1999.

[52] G. E. Eperon, V. M. Burlakov, P. Docampo, A. Goriely, and H. J. Snaith, "Morphological Control for High Performance, Solution-Processed Planar Heterojunction Perovskite Solar Cells," *Advanced Functional Materials,* vol. 24, no. 1, pp. 151-157, 2014.

[53] F. Capasso, "Band-gap engineering- From physics and materials to new semiconductor devices," *Science,* vol. 235, no. 4785, pp. 172-176, 1987.

[54] A. Brehier, R. Parashkov, J.-S. Lauret, and E. Deleporte, "Strong exciton-photon coupling in a microcavity containing layered perovskite semiconductors," *Applied physics letters,* vol. 89, no. 17, pp. 171110-171110-3, 2006.

[55] R. Holmes and S. Forrest, "Strong exciton–photon coupling in organic materials," *Organic Electronics,* vol. 8, no. 2, pp. 77-93, 2007.

[56] M. Kulbak *et al.*, "Cesium enhances long-term stability of lead bromide perovskite-based solar cells," *The journal of physical chemistry letters,* vol. 7, no. 1, pp. 167-172, 2015.

[57] S. D. Stranks *et al.*, "Electron-hole diffusion lengths exceeding 1 micrometer in an organometal trihalide perovskite absorber," *Science,* vol. 342, no. 6156, pp. 341-344, 2013.

[58] X. Bao, L. Sun, W. Shen, C. Yang, W. Chen, and R. Yang, "Facile preparation of TiO X film as an interface material for efficient inverted polymer solar cells," *Journal of Materials Chemistry A,* vol. 2, no. 6, pp. 1732-1737, 2014.

[59] A. Yella, L.-P. Heiniger, P. Gao, M. K. Nazeeruddin, and M. Grätzel, "Nanocrystalline rutile electron extraction layer enables low-temperature solution processed perovskite photovoltaics with 13.7% efficiency," *Nano letters,* vol. 14, no. 5, pp. 2591-2596, 2014.

[60] L. Etgar *et al.*, "Mesoscopic CH3NH3PbI3/ TiO2heterojunction solar cells," *Journal of the American Chemical Society,* vol. 134, no. 42, pp. 17396-17399, 2012.

[61] K. Zhu, N. R. Neale, A. Miedaner, and A. J. Frank, "Enhanced charge-collection efficiencies and light scattering in dye-sensitized solar cells using oriented TiO2 nanotubes arrays," *Nano letters,* vol. 7, no. 1, pp. 69-74, 2007.

[62] Y. Sun, J. H. Seo, C. J. Takacs, J. Seifter, and A. J. Heeger, "Inverted polymer solar cells integrated with a low-temperature-annealed sol-gel-derived ZnO film as an electron transport layer," *Advanced Materials,* vol. 23, no. 14, pp. 1679-1683, 2011.

[63] X. Wang, L. Zhi, and K. Müllen, "Transparent, conductive graphene electrodes for dye-sensitized solar cells," *Nano letters,* vol. 8, no. 1, pp. 323-327, 2008.

[64] K. Ihm *et al.*, "Number of graphene layers as a modulator of the open-circuit voltage of graphene-based solar cell," *Applied Physics Letters,* vol. 97, no. 3, p. 032113, 2010.

[65] A. K. Geim and K. S. Novoselov, "The rise of graphene," *Nature materials,* vol. 6, no. 3, pp. 183-191, 2007.

[66] J. T.-W. Wang *et al.*, "Low-temperature processed electron collection layers of graphene/TiO2 nanocomposites in thin film perovskite solar cells," *Nano letters,* vol. 14, no. 2, pp. 724-730, 2013.

[67] H. Kim, K.-G. Lim, and T.-W. Lee, "Planar heterojunction organometal halide perovskite solar cells: roles of interfacial layers," *Energy & Environmental Science,* vol. 9, no. 1, pp. 12-30, 2016.

[68] H.-S. Kim *et al.*, "Lead iodide perovskite sensitized all-solid-state submicron thin film mesoscopic solar cell with efficiency exceeding 9%," *Scientific reports,* vol. 2, p. 591, 2012.

[69] E. A. Gaml *et al.*, "Alternative benzodithiophene (BDT) based polymeric hole transport layer for efficient perovskite solar cells," *Solar Energy Materials and Solar Cells,* vol. 168, pp. 8-13, 2017.

[70] Y. Zhou, F. Li, S. Barrau, W. Tian, O. Inganäs, and F. Zhang, "Inverted and transparent polymer solar cells prepared with vacuum-free processing," *Solar Energy Materials and Solar Cells,* vol. 93, no. 4, pp. 497-500, 2009.

[71] O. Bubnova and X. Crispin, "Towards polymer-based organic thermoelectric generators," *Energy & Environmental Science,* vol. 5, no. 11, pp. 9345-9362, 2012.

[72] T. Xu and Q. Qiao, "Conjugated polymer–inorganic semiconductor hybrid solar cells," *Energy & Environmental Science,* vol. 4, no. 8, pp. 2700-2720, 2011.

[73] S. Tokito, K. Noda, and Y. Taga, "Metal oxides as a hole-injecting layer for an organic electroluminescent device," *Journal of Physics D: Applied Physics,* vol. 29, no. 11, p. 2750, 1996.

[74] J. Meyer, S. Hamwi, M. Kröger, W. Kowalsky, T. Riedl, and A. Kahn, "Transition metal oxides for organic electronics: energetics, device physics and applications," *Advanced Materials,* vol. 24, no. 40, pp. 5408-5427, 2012.

[75] M. D. Irwin, D. B. Buchholz, A. W. Hains, R. P. Chang, and T. J. Marks, "p-Type semiconducting nickel oxide as an efficiency-enhancing anode interfacial layer in polymer bulk-heterojunction solar cells," *Proceedings of the National Academy of Sciences,* vol. 105, no. 8, pp. 2783-2787, 2008.

[76] J. Liu, S. Shao, G. Fang, B. Meng, Z. Xie, and L. Wang, "High-Efficiency Inverted Polymer Solar Cells with Transparent and Work-Function Tunable MoO3-Al Composite Film as Cathode Buffer Layer," *Advanced Materials,* vol. 24, no. 20, pp. 2774-2779, 2012.

[77] L. Kelvin, "V. Contact electricity of metals," *The London, Edinburgh, and Dublin Philosophical Magazine and Journal of Science,* vol. 46, no. 278, pp. 82-120, 1898.

[78] W. Melitz, J. Shen, A. C. Kummel, and S. Lee, "Kelvin probe force microscopy and its application," *Surface Science Reports,* vol. 66, no. 1, pp. 1-27, 2011.

[79] S. Magonov and J. Alexander, "Advanced Atomic force microscopy: Exploring measurements of local electric properties," *Application Note, Agilent Technologies, Inc,* 2008.

[80] W. M. Lin, D. Bozyigit, O. Yarema, and V. Wood, "Transient Photovoltage Measurements in Nanocrystal-Based Solar Cells," *The Journal of Physical Chemistry C,* vol. 120, no. 23, pp. 12900-12908, 2016.

[81] K. Sun, J. Chang, F. H. Isikgor, P. Li, and J. Ouyang, "Efficiency enhancement of planar perovskite solar cells by adding zwitterion/LiF double interlayers for electron collection," *Nanoscale,* 10.1039/C4NR05975A vol. 7, no. 3, pp. 896-900, 2015.